SCANNING FORCE MICROSCOPY SIMULATIONS OF NANOPARTICLES ON INSULATING SURFACES

Olli Pakarinen

Department of Engineering Physics
Helsinki University of Technology
Espoo, Finland

Dissertation for the degree of Doctor of Science in Technology to be presented with due permission of the Faculty of Information and Natural Sciences for public examination and debate in Auditorium E at Helsinki University of Technology (Espoo, Finland) on the 15th of February, 2008, at 13 o'clock.

Dissertations of Department of Engineering Physics
Helsinki University of Technology
ISSN 1455-1802

Dissertation 152 (2008):
Olli Pakarinen: Scanning force microscopy simulations of nanoparticles on insulating surfaces

Opponent:
Dr. Lev Kantorovich, King's College London, United Kingdom

Pre-examiners:
Prof. Hannu Häkkinen, University of Jyväskylä, Finland
Ass. Prof. Jeppe Lauritsen, University of Aarhus, Denmark

ISBN 978-951-22-9221-9 (print)
ISBN 978-951-22-9222-6 (electronic)

Picaset Oy
Helsinki 2008

ABSTRACT OF DOCTORAL DISSERTATION	HELSINKI UNIVERSITY OF TECHNOLOGY P. O. BOX 1000, FI-02015 TKK http://www.tkk.fi

Author Olli Pakarinen

Name of the dissertation

Scanning force microscopy simulations of nanoparticles on insulating surfaces

Manuscript submitted	12.11.2007	Manuscript revised	25.1.2008

Date of the defence 15.2.2008 at 13 o'clock, TKK main building, Otakaari 1, lecture hall E

☐ Monograph ☒ Article dissertation (summary + original articles)

Faculty	Faculty of Information and Natural Sciences
Department	Department of Engineering Physics
Field of research	Computational materials physics
Opponent(s)	Dr. Lev Kantorovich, King's College London
Supervisor	Acad. Prof. Risto Nieminen
Instructor	Dr. Adam Foster

Abstract

Scanning (atomic) force microscopy (SFM/AFM) is a surface science method capable of imaging surfaces with atomic resolution. SFM is a local probe method, closely related to other scanning probe microscopy methods like scanning tunneling microscopy (STM). Dynamic SFM studied in this thesis utilizes a very sharp tip at the end of an oscillating cantilever, and forms images of surfaces by measuring the tip-sample interaction while scanning very close (typically less than 1 nm) above the surface.

Computational work is typically needed for interpretation of experimental SFM results, as the output of the instrument depends strongly on the atomic structure of the tip apex, unknown in most experiments. Simulations also open a window to view the atomic scale processes which determine the outcome of the experiment, and can show new ways to optimise the use of SFM.

This dissertation presents computational simulations of scanning force microscopy, focusing on imaging nanoscale particles on insulating surfaces. Numerical methods to calculate the tip-sample interactions are developed. Simulations of atomic resolution contrast in SFM imaging are performed utilizing density functional theory as well as semiclassical methods. Larger scale simulations focusing on the tip convolution problem are made possible with the development of a numerical code calculating van der Waals interaction between arbitrarily shaped objects. The effect of humidity on particle-surface interaction is studied by development of another numerical code modeling the capillary forces.

The described work generates new understanding of image formation in SFM, and of the change of behavior of capillary forces at the nanoscale. A new application to utilize the constant height mode of SFM to greatly diminish the tip convolution effect is presented, and its success is explained with simulations.

Keywords Force microscopy, SFM, AFM, nc-AFM, DFM, nanoclusters

ISBN (printed)	978-951-22-9221-9	ISSN (printed)	1455-1802
ISBN (pdf)	978-951-22-9222-6	ISSN (pdf)	
Language	English	Number of pages	67 p. + app. 58 p.

Publisher Department of Engineering Physics, Helsinki University of Technology

Print distribution

☒ The dissertation can be read at http://lib.tkk.fi/Diss/9789512292226/

VÄITÖSKIRJAN TIIVISTELMÄ	TEKNILLINEN KORKEAKOULU PL 1000, 02015 TKK http://www.tkk.fi

Tekijä Olli Pakarinen

Väitöskirjan nimi

Atomivoimamikroskopian mallintaminen: nanohiukkaset eristepinnoilla

Käsikirjoituksen päivämäärä	12.11.2007	Korjatun käsikirjoituksen päivämäärä	25.1.2008

Väitöstilaisuuden ajankohta 15.2.2008 klo 13, Teknillisen korkeakoulun päärakennus, Otakaari 1, sali E

☐ Monografia ☒ Yhdistelmäväitöskirja (yhteenveto + erillisartikkelit)

Tiedekunta	Informaatio- ja luonnontieteiden tiedekunta
Laitos	Teknillisen fysiikan laitos
Tutkimusala	Laskennallinen materiaalifysiikka
Vastaväittäjä(t)	Dr. Lev Kantorovich, King's College London
Työn valvoja	Akatemiaprofessori Risto Nieminen
Työn ohjaaja	Dr. Adam Foster

Tiivistelmä

Atomivoimamikroskopia (SFM/AFM) on pintatutkimustekniikka, jolla pintoja voidaan kuvantaa yksittäiset atomit erottavalla resoluutiolla. Tässä väitöstyössä tutkittu dynaaminen SFM perustuu oskilloivaan kannatinvarteen kiinnitettyyn erittäin terävään mittakärkeen. Mittakärjen ja tutkittavan pinnan välisen vuorovaikutuksen voimakkuus pienellä (tyypillisesti alle 1 nm) etäisyydellä saadaan mitattua varren oskillointitaajuuden muutoksesta, ja pinta kuvannettua mittaamalla taajuutta pinnan yllä paikan funktiona. Instrumentti muistuttaa läheisesti tunnelointimikroskooppia (STM), mutta erilaisen toimintaperiaatteensa vuoksi sillä on laajempi käyttöalue.

Laskennallista tutkimusta tarvitaan kokeellisten SFM-tulosten tulkintaan, sillä instrumentin tuottamat tulokset riippuvat voimakkaasti mittakärjen atomirakenteesta, joka lähes kaikissa kokeissa on tuntematon. Simulaatioilla voidaan myös nähdä atomimittakaavan prosesseja, jotka vaikuttavat tuloksiin, sekä kehittää parempia tapoja atomivoimamikroskoopin käyttöön tutkimuksessa.

Tämä väitöskirja esittää, miten atomivoimamikroskooppia voidaan mallintaa numeerisin simulaatioin erityisesti nanokokoisten hiukkasten tutkimuksessa eristepinnoilla. Työ selittää mittakärjen ja tutkittavan pinnan välisen vuorovaikutuksen laskemiseen kehitetyt laskennalliset mallit ja esittelee niiden eri sovelluksia. Atomiresoluution mallinnusta on tässä tutkimuksessa tehty niin kvanttimekaanista tiheysfunktionaaliteoriaa kuin semiklassisia mallejakin käyttäen. Yksittäisiä atomeja suuremmassa mittakaavassa SFM-mittakärjen konvoluutiota (*tip convolution*) mallintavia simulaatioita varten on kehitetty laskentakoodi, jolla van der Waals -vuorovaikutukset voidaan laskea mielivaltaisen muotoisten kappaleiden välillä. Kosteuden vaikutusta on tutkittu työssä kehitetyllä kapillaarivoimia simuloivalla ohjelmalla.

Väitöstyössä esitetyt sovellukset lisäävät SFM:n kuvanmuodostuksen ja -tulkinnan ymmärtämystä ja selittävät kapillaarivoimien käytöksessä nanomittakaavassa ilmenevät erityispiirteet. Mittakärjen ja tutkittavan kohteen konvoluution havaitaan voimakkaasti vähentyvän ja instrumentin erotuskyvyn näin paranevan, kun nanohiukkasia kuvannetaan SFM:n vakiokorkeusmoodissa. Havaitun ilmiön alkuperä myös tulkitaan simulaatioiden avulla.

Asiasanat atomivoimamikroskopia, SFM, AFM, nc-AFM, DFM, nanohiukkaset

ISBN (painettu)	978-951-22-9221-9	ISSN (painettu)	1455-1802
ISBN (pdf)	978-951-22-9222-6	ISSN (pdf)	
Kieli	englanti	Sivumäärä	67 s. + liitteet 58 s.

Julkaisija Teknillisen fysiikan laitos, Teknillinen korkeakoulu

Painetun väitöskirjan jakelu

☒ Luettavissa verkossa osoitteessa http://lib.tkk.fi/Diss/9789512292226/

Affiliation

Author
Olli Pakarinen
Department of Engineering Physics
Helsinki University of Technology
Espoo, Finland
opa@fyslab.hut.fi

Opponent
Dr. Lev Kantorovich
Department of Physics
King's College London
London, United Kingdom
lev.kantorovitch@kcl.ac.uk

Supervisor
Dr. Adam Foster
Department of Engineering Physics
Helsinki University of Technology
Espoo, Finland
asf@fyslab.hut.fi

Supervisor
Acad. Prof. Risto Nieminen
Department of Engineering Physics
Helsinki University of Technology
Espoo, Finland
Risto.Nieminen@hut.fi

Pre-examiner
Prof. Hannu Häkkinen
Department of Physics
Nanoscience Center
University of Jyväskylä
Jyväskylä, Finland
hannu.hakkinen@phys.jyu.fi

Pre-examiner
Ass. Prof. Jeppe Lauritsen
Department of Physics and Astronomy
University of Aarhus
Århus, Denmark
jvang@phys.au.dk

Preface

This thesis has been prepared in the Computational Nanoscience group of Laboratory of Physics, Helsinki University of Technology, during 2003-2008. I wish to thank Academy Professor Risto Nieminen for the opportunity to work in the COMP group and for the supervision.

I wish to express my gratitude to Dr. Adam Foster for his supervision. He has been guiding me both in the scientific work and practical issues with endless patience and support, giving fresh scientific ideas to follow in research without suffocating free thinking.

I would also like to acknowledge my collaborators and colleagues at TKK, CRMCN-CNRS Marseille, and Osaka University, most of the work presented here has been done in close collaboration with other scientists, both experimental and theoretical.

This research has been supported by the Academy of Finland Centre of Excellence Program (2000-2005, 2006-2011), and by the Finnish Funding Agency for Technology and Innovation (TEKES) via the PINTA Research Program. Main part of the computer resources have been offered by CSC, the Finnish IT center for science, owned by the Ministry of Education. This financial support is gratefully acknowledged.

Finally, I would like to thank my parents and especially my wife Hanna and our lovely daughter Enni for the best of support and care.

Espoo, January 2008

Olli Pakarinen

Contents

Abstract i
Tiivistelmä iii
Affiliation v
Preface vii
Contents viii
List of publications xi
List of abbreviations and units xii
List of symbols xiii

1 Introduction **1**

2 Scanning force microscopy **3**
2.1 Introduction to SFM and STM 4
2.2 Experimental setup 6
2.3 Energy dissipation 8
2.4 Tip convolution 8
2.5 Topographic and constant height modes 9
2.6 Site-specific force spectroscopy 10

3 Simulating SFM **13**
3.1 Introduction 13
3.2 Relevant forces in SFM 14
    3.2.1 Chemical forces 14
    3.2.2 Van der Waals forces 15
    3.2.3 Capillary forces 16
    3.2.4 Other forces relevant for some SFM systems 16
3.3 Simulating SFM imaging 17
    3.3.1 Tip models 17
    3.3.2 Cantilever oscillation properties 18
    3.3.3 Producing simulated SFM images from frequency shift data . . . 19
    3.3.4 Accuracy of SFM simulations 20

Calculating tip-surface interactions **21**
3.4 Density functional theory 21
3.4.1 Introduction to DFT 21
3.4.2 Approximations: exchange-correlation functionals and pseudopotentials 23
3.4.3 Tip-sample interactions in DFT 24
3.4.4 SIESTA: DFT code for solids 25
3.5 Atomistic simulations with pair-potentials using MARVIN2 26
3.6 Volume element code for van der Waals interactions 26
3.7 Simulating capillary forces 27
3.7.1 Introduction to capillary forces 28
3.7.2 Numerical method 31
3.7.3 Conclusions 32

4 Simulating atomic resolution SFM imaging **33**
4.1 $TiO_2(110)$ studied with atomistic potentials 34
4.2 KBr(001) surface studied with density functional theory 36
4.3 Imaging gold nanoclusters on KBr(001) 38

5 Tip convolution in nanocluster imaging **41**
5.1 Gold nanoclusters on KBr(001) and HOPG 41
5.2 Pd nanoclusters on MgO(001) 43
5.3 Explaining the success of constant height mode 45

6 Conclusions and outlook **47**

Bibliography **49**

List of publications

This thesis consists of an overview and the following publications:

- **I** A. S. Foster, O. H. Pakarinen, J. M. Airaksinen, J. D. Gale, and R. M. Nieminen, *Simulating atomic force microscopy imaging of the ideal and defected TiO2 (110) surface*, Physical Review B **68**, 195410 (2003)
- **II** O. H. Pakarinen, A. S. Foster, M. Paajanen, T. Kalinainen, J. Katainen, I. Makkonen, J. Lahtinen, and R. M. Nieminen, *Towards an accurate description of the capillary force in nanoparticle-surface interactions*, Modelling and Simulation in Materials Science and Engineering **13**, 1175 (2005)
- **III** C. Barth, O. H. Pakarinen, A. S. Foster, and C. R. Henry, *Imaging nanoclusters in the constant height mode of the dynamic SFM*, Nanotechnology **17**, S128 (2006)
- **IV** O. H. Pakarinen, C. Barth, A. S. Foster, and C. R. Henry, *High-resolution scanning force microscopy of gold nanoclusters on the KBr (001) surface,* Physical Review B **73**, 235428 (2006)
- **V** Olli H. Pakarinen, Clemens Barth, Adam S. Foster, and Claude R. Henry, *Imaging the real shape of nanoclusters in scanning force microscopy*, Journal of Applied Physics (in press)

The author has had an active role in all the phases of the research reported in this thesis. He has developed the methods of calculation and computer codes used in Publications II, III and V. The author has performed all the calculations in Publications II-V, and the calculations with oxide tips in Publication I, and has participated in planning the calculations and interpretation of both experimental and computational results. He has written the first draft of Publications II and IV, and partly those of Publications III and V.

List of abbreviations

DFT	density functional theory
GGA	generalized gradient approximation
LCAO	linear combination of atomic orbitals
LDA	local density approximation
SFM	scanning force microscopy/microscope
STM	scanning tunneling microscopy/microscope
UHV	ultra-high vacuum, $p < 10^{-9}$ Torr $\approx 1.33 \cdot 10^{-12}$ bar
vdW	van der Waals interaction

Units

eV	electron volt, $1.602177{\cdot}10^{-19}$ J
K	Kelvin
μm	micrometer, 10^{-6} m
nm	nanometer, 10^{-9} m
nN	nanonewton, 10^{-9} kgm/s^2
pm	picometer, 10^{-12} m
Å	Ångström, 10^{-10} m $= 0.1$ nm

List of symbols

A	oscillation amplitude, area
B	magnetic flux density
C	capacitance
C_6	London constant for dispersion force
d	distance/separation
F	force
f	frequency
Δf	frequency shift
H	Hamaker constant
$\hat{H}$	Hamiltonian operator
H_r	relative humidity
h	height
k	spring constant
k_B	Boltzmann constant
m	magnetic moment
n	electronic density
p	pressure
Q, q	point charge
R	tip radius
r	distance/separation, radius
$\hat{T}$	kinetic energy (operator)
T	temperature
U	potential energy, contact potential
V	(interaction) potential, volume
v_0	molecular volume
z	separation in vertical direction
α	damping constant
γ	surface tension
ρ	density, number density
θ	contact angle
ϕ	(interaction) potential
Ψ	wave function

Chapter 1

Introduction

In this thesis scanning force microscopy (SFM) is introduced as a technique to image surfaces and nanoscale structures at atomic resolution, and its capabilities and challenges are discussed from a computational point of view. The method has emerged as one of the most powerful tools in studying surface phenomena in atomic detail, and the research performed by SFM is continuously increasing its scope from measuring adhesion and imaging simple surfaces to complex systems involving clusters on surfaces, chemical reactions, manipulation of single atoms, construction and characterization of nanodevices, and biophysical systems. The SFM principle is also utilized in numerous concepts of future technology, for example functioning as accurate gas sensors [1] or in IBM's Millipede project [2], as a possible replacement of today's magnetic memory hard disks by a superior, cantilever-read MEMS-based memory, exceeding 1 Tb per square inch data density. In scanning force microscopy research, experimental and theoretical or computational work intermingle very strongly, as the powerful instrument has an Achilles' heel - a crucial part of the instrument itself is unknown in most experiments, and careful interpretation is needed to understand the images it produces. This can usually be done only by comparing experimental and theoretical results.

SFM is also known as atomic force microscopy (AFM), but the name SFM is preferred in this thesis, as the name links the instrument to its 'family' of local probes, scanning probe microscopies (SPM), and to its sibling, scanning tunneling microscope (STM). Moreover, the certain type of SFM mainly considered in this thesis is called *dynamic SFM* [3–6], also known as nc-AFM (nc for non-contact) or DFM (dynamic force microscopy.) In dynamic SFM the tip of the instrument is oscillated above the surface, and the measurement signal, strength of the interaction between surface and tip, is read from the change of oscillation frequency of the cantilever that holds the tip.

The methods presented in the thesis have been applied to study different problems in collaboration with experimental SFM work, presented in the five articles in the Appendices. In Article **I**, imaging $TiO_2(110)$ surfaces with atomic resolution is studied, using both *ab initio* and shell model methods. Article **II** concentrates on simulating capillary forces, important for systems including humidity (such as SFM adhesion experiments made in air), and gives a detailed study of factors affecting the phenomenon in length scales relevant for SFM. In Article **IV** gold nanoclusters grown on KBr(001) surface are studied by density functional theory, concentrating both on atomic resolution imaging of the surface and nanoclusters, and on electronic properties and nucleation of the clusters on surface. In Articles **III** and **V** the effect of tip convolution on imaging metal nanoclusters, Au on highly ordered pyrolytic graphite (HOPG) and NaCl(001), and Pd on MgO, respectively, is studied with classical simulations, and a new method to increase imaging contrast by utilizing constant height mode SFM imaging is proposed.

The structure of the thesis is following: Chapter 2 introduces the scanning force microscope (SFM), its basic operation and experimental setup. Chapter 3 focuses on computational details - how to model SFM in general - introducing methods to calculate tip-sample interactions, and explaining how this information can be used to produce simulated images of surfaces, with direct comparability to experimental images. Chapter 4 focuses on atomic resolution SFM simulations, both on plain surfaces and metal nanoclusters. Simulations on TiO_2 present an example of utilizing classical potentials for atomistic calculations, whereas simulations on the KBr(001) surface and gold nanoclusters demonstrate the use of density functional theory in SFM studies. Chapter 5 presents a novel method of utilizing the SFM constant height mode for imaging clusters on surfaces with increased accuracy. The simulations explaining the physical origin of the phenomenon are discussed. Finally, Chapter 6 summarizes the contents.

Chapter 2

Scanning force microscopy

Standard surface science methods work on a principle of forming images of the surface by targeting the sample with particles - photons or electrons - relatively high in energy, and measuring the reflected or scattered light or electrons by macroscopically large (∼1 cm - 1 m) detectors. Improving their resolution to atomic scale has proven very difficult - often these methods work by giving averages of the wanted quantity over a rather large surface area, and often the methods are destructive to the sample due to high energies. Scanning force microscope, for one, is a *local probe*, which operates with a different principle: The measurement instrument ideally has one atom at the end of a sharp tip, moving continuously over the surface, and forming the image with the smallest possible interaction with the surface still enabling detection (see figure 2.1.) Thus the local probe is capable of measuring tiny details like changes of electronic structure in single atoms and also manipulating atoms one by one.

There are at least four technical requirements a working local probe instrument must fulfill [8]:

- strong distance dependence of the interaction
- close proximity of the probe and object
- stable positioning device
- very sharp probe for true atomic resolution instead of averages

The first requirement arises from the fact that to achieve atomic resolution, there must be a measurable change in signal when the probe-sample distance changes by less than

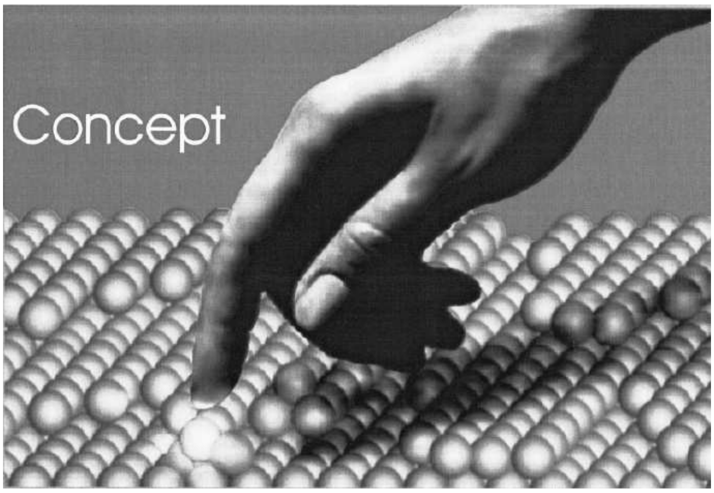

Figure 2.1: *Concept of local probes. The instrument is of the size of atoms it measures, and brought nearly into contact with single atoms to "feel" them. (After [7].)*

one atomic diameter. Only chemical interactions (change of force from 0.2 to 3.0 nN within 0.2 nm distance) and tunneling current (change of one order of magnitude within 0.1 nm distance) fulfill this requirement [8]. The second requirement follows from the first: the very short ranged interactions can only be measured at a tip-sample separation of less than one nanometer. This imposes very tough requirements on probe position control and stability against vibrations, the third listed requirement, to maintain the probe at the correct imaging distance without crashing to the surface. Stable positioning is also needed to scan the surface in a controlled fashion to form images of surface features. The fourth and final requirement is needed for *true atomic resolution*: A flat probe will average the interaction over a large number of surface atoms, and at best produce images that show atomic periodicity of the lattice. The technical requirement for true atomic resolution is, however, to actually see single atom-sized details like point defects on surfaces, and for this a tip with a curvature radius between 10 and 100 nm, and an atomically sharp apex is typically needed.

2.1 Introduction to SFM and STM

SFM was developed by Binnig, Quate and Gerber in 1986 [9], and in the same year Binnig and Rohrer shared the Physics Nobel Prize [10] for their earlier invention, STM, which was first developed in 1982 [11], and has since been very successful in imaging [12,13] and manipulating [14] surfaces. The STM instrument has a very sharp tip above the imaged surface, close enough for electrons to tunnel across the vacuum gap when a bias voltage is applied between the tip and the sample, and this tunnelling current can be used to draw an image of the surface. As the tunnelling current decays exponentially with distance, the surface is imaged mainly by the very last atom of the tip apex, which relatively routinely allows atomic resolution imaging of surfaces.

However successful STM has become on studying suitable systems, it has severe drawbacks that limit its use. Since the imaging is based on measuring the tunnelling current between the tip and sample, both need to be made of conducting materials, and therefore only metallic or semiconductor samples can be studied. This rules out all the systems based on insulating materials, important for many areas of nanoscale sciences, for fields such as catalysis, nanoelectronics, as well as for biological and medical applications [15–18]. It is possible to study very thin layers (a few monolayers) of insulators on top of a conducting substrate, but in these cases the properties of the system are somewhat different from a realistic bulk insulator system [19]. Secondly, as STM is imaging the electronic structure of the sample surface, the obtained images often do not resemble the physical topography of the surface, *i.e.* the details seen in images do not necessarily match to surface atoms, but sites where the local density of states (LDOS) between the tip and sample Fermi levels (contributing to the tunnelling current) differs from the surroundings. The fact that STM images only the most loosely bound electrons of atoms, close to the Fermi level, may also limit its resolution below the ultimate resolution of SFM [20].

SFM was developed to tackle these problems, as despite its similarities with STM - a very sharp tip measuring local surface topography at atomic resolution - SFM works on a different principle. The measured physical signal in SFM is the interaction between the tip and sample, which has several advantages over tunnelling current:

- interaction is measurable for all kinds of surfaces - insulators, semiconducting and metallic
- tips need not be conducting, and thus can be easily integrated with cantilevers, or utilize insulating materials or molecules
- interaction is usually a more reliable signal of the real surface corrugation than current measuring electronic structure of the surface

On the other hand, measuring interaction instead of the tunnelling current has some drawbacks:

- interaction is clearly longer-ranged, and a large part of the tip contributes to imaging, instead of the last atom of the tip apex in STM, increasing the need for tip sharpness
- unlike tunnelling current, the tip-surface interaction is not monotonic with distance, and therefore it is harder to obtain stable imaging at a fixed signal point close to the surface, and tip-surface collisions often harm the system
- information on the electronic structure is lacking

Therefore STM and SFM can be described as partly complementary methods, capable of providing different information of surfaces.

2.2 Experimental setup

Scanning force microscopy is based on a very sharp tip at the end of a deflecting or oscillating cantilever. This deflection can be measured in a number of ways, usually a laser beam is reflected from the back of the cantilever, coated for example with gold, to a segmented photodiode. The cantilever is attached into a positioning piezo, which allows scanning two-dimensional images over the sample with very accurate positioning. In the initial SFM experiments the so-called *contact mode* was used, where the SFM tip is being pressed against the imaged surface. Since the mode is rather destructive to the surface and true atomic resolution is lacking, another imaging mode without hard contact with the surface is preferable, to minimise change of material between the tip and the surface. The cantilever's tendency to jump-to-contact whenever the tip-surface interaction overcomes the cantilever stiffness, if imaging close above the surface, prevents static imaging. Another imaging mode, *dynamic* SFM (a.k.a. non-contact AFM, DFM) has proven successful. As shown in figure 2.2, in dynamic SFM the cantilever is oscillated above the surface with a certain amplitude A_0, typically 5-100 nm, and the elastic force of the cantilever prevents jump-to-contact if the following conditions are met [21]:

$$\left|\frac{d^2\phi}{dz^2}\right|_{max} < k, \tag{2.1}$$

$$\left|-\frac{d\phi}{dz}\right|_{max} < kA_{0,} \tag{2.2}$$

where ϕ is the interaction potential, z is the separation between tip and surface, and k is the cantilever spring constant. Usually the tip oscillation is controlled with frequency modulation (FM) mode, where the cantilever with an eigenfrequency f_0 (typically 50-200 kHz) is kept oscillating at a constant amplitude by a feed-back loop. At a phase shift $\theta = \pi/2$ the free cantilever oscillates at frequency $f = f_0$. During imaging, close to the surface, the tip-surface interaction causes a deviation from this frequency (negative for attractive interaction), called frequency shift Δf (see figure 2.2), and topographic images of the surface can be formed by varying the tip-surface distance to keep Δf at a constant value.

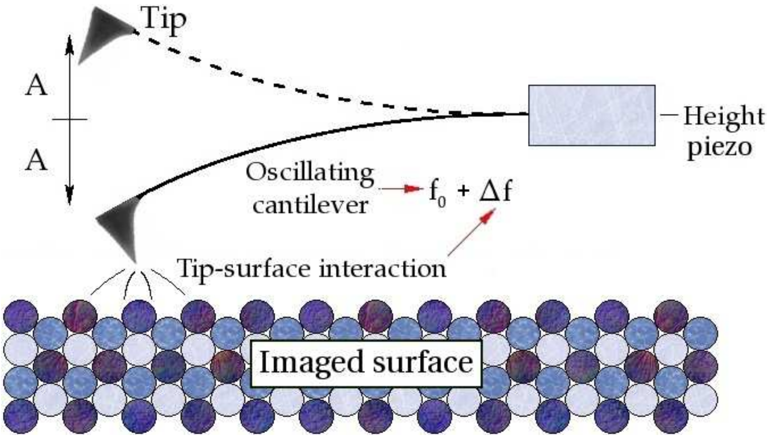

Figure 2.2: *Operating principle of the dynamic SFM: The interaction between the surface and the sharp tip changes the oscillation frequency of the cantilever, and an image of the surface can be generated from this frequency shift.*

As the SFM cantilever must detect tiny changes in tip-surface interaction (well below 1 nN), imaging just a few Ångströms from the surface, the instrument is very delicate and susceptible to external vibrations. Therefore the whole instrument is well damped, often suspended by springs. To accurately control the surfaces imaged and to avoid contaminations, the measurements are usually performed in ultra-high vacuum (UHV, $p \approx 10^{-12}$ bar), although in some applications air or water (for example in biophysics) is the preferable medium [22]. Typically the measurements are made at room temperature, but to further limit thermal noise and movement of surface atoms and molecules, some SFM setups can be cooled to liquid nitrogen (77 K) or liquid helium (4.2 K) temperatures, allowing extremely high-quality imaging to be performed [23]. Some experiments utilize a sub-Ångström oscillation amplitude of especially stiff cantilevers and higher harmonics of the oscillation [24] to further improve sensitivity to the short-range interactions, and therefore also the resolution into sub-atomic limit [20]. The technique is also advantageous for imaging in a liquid environment [22].

2.3 Energy dissipation

To maintain constant oscillation amplitude, an SFM feedback loop applies an excitation to the cantilever, A_{exc}. Also this excitation amplitude can be used as a measurement signal producing images, instead of the frequency shift, and it has an advantage similar to the tunnelling current in STM: the signal is monotonic with distance, offering very good tip-sample distance control. On the other hand, the dissipation signal has a very strong dependence on atomic structure of the tip, and thus the contrast obtained from A_{exc} varies from sharp to poor. This also means that the signal shows clearly the occurrence of tip changes [25].

The mechanism behind atomic-scale dissipation has been clarified only recently, resolving the dispute between two possible explanations. The first model to try to explain the experiments was *stochastic friction force* mechanism [26, 27], based on friction caused by thermal fluctuations of atoms near contact, behavior similar to a Brownian particle in a fluid reservoir. Computational results have shown that the dissipation caused by the mechanism ($10^{-8} - 10^{-9}$eV per oscillation cycle), can not reproduce the experimental dissipation energies (0.01-1 eV per cycle) [28]. The *adhesion hysteresis* mechanism is thus the only candidate producing dissipation energies in good agreement with experiment [29]. In this model dissipation is caused by the SFM tip following different paths on approach and retraction, inducing reversible changes in atomic structure of tip and sample, which results in a double-well potential in the tip-sample potential energy surface.

2.4 Tip convolution

When SFM is used to image small three-dimensional surface features such as step edges or clusters on a surface, the radius of the tip apex starts to affect the images. If the instrument is used in the typical *topographic mode*, in which the cantilever z-piezo movement follows contours of the surface, the obtained shapes are not determined purely by the shape of the imaged object, but also the profile of the tip. For imaged objects clearly larger than the tip radius this is not a serious problem, but for objects of the same or smaller size than the tip, the obtained images can represent the shape of the tip, not of the surface. This effect is known as tip convolution.

Figure 2.3 shows the effect of tip convolution for a parabolic tip and a cubic surface asperity of similar dimensions. The tip apex position (shown in red) forms the topographic image of the asperity, but the advancing front profile (in black), meeting the asperity before the apex, forces the obtained profile to be clearly wider and more rounded than the actual asperity profile.

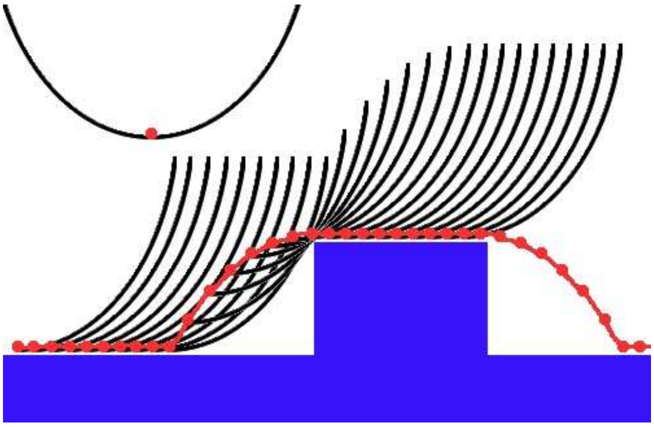

Figure 2.3: *Tip convolution: a parabolic tip imaging a cubic surface asperity. The advancing front profile of the tip is shown in black, and obtained topographic signal from the tip apex position in red.*

To avoid tip convolution problems, the tip should be as sharp as possible, but for imaging objects of a few nanometers in size, the tip will in any case be of a roughly similar size as the imaged object, and therefore the effect cannot easily be avoided. In some cases it is possible to image the tip apex shape, and after this is known, to calculate out the broadening in images. Another solution is to use SFM in the *constant height mode*.

2.5 Topographic and constant height modes

Scanning force microscopy is typically performed in the *topographic mode*, in which the z-piezo of the instrument, modulating the tip-sample separation, follows the contour of constant frequency shift on the surface, and the z-piezo height is recorded as the imaging signal above each point of the surface. This way a topographic image of the surface is obtained, in principle showing the height variations of the surface, but in high resolution imaging also affected by chemical composition of the surface.

Another possibility is to use the instrument in the *constant height mode*, in which the tip oscillates at a constant height above the surface, and the frequency shift is obtained as the measurement signal above surface. The mode allows very fast scanning speeds

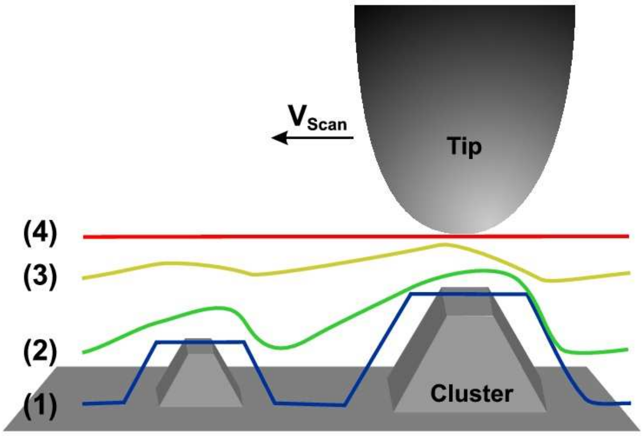

Figure 2.4: *Path of the lowest point in SFM tip oscillation, while scanning the surface in topographic mode (1), and in constant height mode (4). Curves (2) and (3) correspond to intermediate behavior.*

on surfaces, as the z-control loop is not needed, typically up to 50 Hz, at least one order of magnitude faster than in the topographic mode. This is important for imaging surface processes in real time, especially for biophysical studies. The scanning path of the lowest point of tip oscillation in different imaging modes is explained in figure 2.4, where path (1) corresponds to the topographic mode, and path (4) to the constant height mode.

One further advantage of the constant height mode is that by using it, a combined STM/SFM instrument can measure both the tunnelling current and the frequency shift simultaneously [30]. This is not otherwise possible without errors, since topographic modes of STM and SFM are not compatible, *i.e.* the contour of constant current is not a contour of constant frequency shift caused by tip-sample interaction, whereas the constant height mode is an "eigenstate" of both instruments. A combined STM/SFM can be a very powerful tool, giving simultaneous information about both physical topography and electronic structure of the surface.

2.6 Site-specific force spectroscopy

To identify the atomic species on a surface, comparing simulated SFM images to experiment is not always enough. Many surfaces give such a symmetric image regardless of tip termination, that another method to distinguish the nature of the tip apex and surface species is needed. In site-specific force spectroscopy the SFM instrument measures continuous frequency shift - distance curves over well-specified surface sites, and from these curves the short-range interaction over different surface sites can be extracted by subtracting a fitted long-range part from the overall interaction, and compared to simulated force-distance curves. This is in principle a big advantage: the short-range interaction is directly comparable to computational tip-surface interaction simulated by *ab initio* methods, and can lead to unambiguous recognition of atomic species on the surface [31]. The technique is very susceptible to experimental noise, thermal drift and atomic instabilities, and therefore only possible on well-built systems, often at low temperature.

Chapter 3

Simulating SFM

3.1 Introduction

To model scanning force microscopy imaging, several different aspects of the instrument need to be simulated. The heart of the computational effort is in any case the simulation of tip-sample interaction, which is the basic signal that controls the instrument, and determines what type of an image we obtain from the sample.

In dynamic SFM this interaction is not measured in a direct way, however, but instead the frequency shift it causes to the cantilever oscillation is used as the measurement signal. This shift (Δf) is determined by the oscillatory properties of the SFM cantilever, as well as the tip-sample interaction over the oscillation cycle. Therefore, to model SFM imaging also these cantilever properties like cantilever stiffness k, oscillation amplitude A and frequency f need to be modeled, as well as long-range interactions like possible image forces and interaction with the macroscopic part of the tip.

To model the tip-sample interaction, we need to simulate the relevant forces between models of the tip and of the sample surface. The list of relevant forces can differ depending on the system we are studying, and careful analysis is needed to ensure that no relevant components of the interaction are left out of the simulation.

The most crucial aspect of SFM modeling, in general, is to determine a realistic tip model to use. The tip apex composition and shape largely determines the tip-sample interaction, but no methods are in use to determine these properties accurately before the experiment, and therefore different tip models need often to be tested to find one which matches the experiment well enough. Modeling can then be seen as a way to see into the SFM tip and the surface in atomic detail, and to study different aspects such as relaxation of the tip and sample atoms under the interaction, which is not experimentally available.

3.2 Relevant forces in SFM

This section first introduces the forces important for modeling presented in this thesis: chemical forces, van der Waals forces, and capillary forces, for which computational methods are presented in Sections 3.4-3.7. Other interactions may be important for experiments and simulation of SFM as well [32], but are not used in this thesis – these are only shortly introduced.

3.2.1 Chemical forces

The chemical forces are responsible for obtaining atomic resolution with SFM, as only those can separate the chemical species of nearby atoms on the surface [33, 34]. This is because of both their short range and their strong contrast between different elements, whereas other interactions between the tip and the surface only show an average from a larger surface area. Chemical interactions arise from the electrostatic interaction between electrons and nuclei in atoms, polarization and overlap of the electron density.

The types of bonding in a solid can be roughly divided into covalent, ionic, and metallic bonding, depending on the degree of localization of valence orbitals [35]: In ionic bonds the more electronegative atom attracts electron density from the less electronegative atom, and the produced ions interact attractively. In covalent bonds the interacting atoms donate some electronic density spatially directed bonding orbitals between atoms. In metallic bonding, the valence electrons are delocalised around the atomic lattice.

An attractive chemical interaction changes into a repulsive one, when atoms are brought close enough to each other. Repulsion can be caused either by ionic repulsion or the Pauli repulsion, arising from the Pauli exclusion principle, which prevents two same-spin electrons from occupying the same space.

Chemical forces must be treated with atomistic (especially ionic systems) or *ab initio* methods (see Sections 3.5 and 3.4, respectively.)

3.2.2 Van der Waals forces

The van der Waals (vdW) dispersion interaction arises from the coupling of instantaneous fluctuations of the electronic charge in atoms. Dipoles formed in one atom induce dipoles in nearby atoms, and an always attractive[1] force arises from the interaction between dipoles. Other components of van der Waals interaction (induction and orientation forces) are related to permanent dipoles. Usually the largest contribution of vdW interactions comes from the dispersion force (London force), for which the atom-atom potential and force can be written as

$$V_L(r) = -\frac{C_6}{r^6}, \qquad F_L(r) = -\nabla V(r) = -\frac{6C_6}{r^7} \tag{3.1}$$

where C_6 is the London constant, specifying the strength of interaction for the atom pair in case [37]. The short-range interaction between each atom pair adds up to a rather large and longer-ranged force[2], but it is practically impossible to calculate the force between large (by atomic scale standards) bodies simply by summing over all atom pairs. Hamaker [38] showed that the force between two bodies can be obtained by integrating over the volumes, as

$$F_{vdW} = \rho_1\rho_2 \int_{v_2}\int_{v_1} F_L(r)dV_1dV_2, \tag{3.2}$$

where ρ_i and V_i are the atomic number densities and volumes of bodies 1 and 2. The material specific parameters used are typically combined into the *Hamaker constant* of the material,

$$H = \pi^2 C_6\rho_1\rho_2. \tag{3.3}$$

This theory still assumes additivity of atomic interactions, which breaks down as polarizabilities, from which the vdW forces arise from, are determined by complex many-body interactions between several atoms. In Lifshitz theory [39], this problem was circumvented by calculating the interaction between macroscopic bodies from macroscopic optical and dielectric properties of materials, which incorporate the many-body effects. A related effect known as the *Casimir force* [40] is caused by a change of the vacuum expectation value of the energy of the electromagnetic field between two conductors or dielectrics.

---

[1] vdW interaction for two solid bodies is always attractive in vacuum or air. As a general rule for isotropic materials, the static part of the vdW interaction between two bodies is repulsive if the static dielectric constant of the medium between them, ϵ_m, has a value between corresponding values of the bodies, $\epsilon_1 < \epsilon_m < \epsilon_2$ or $\epsilon_2 < \epsilon_m < \epsilon_1$, and the dynamic part is repulsive if the refractive index of the medium is between refractive indices of the bodies, $n_1 < n_m < n_2$ or $n_2 < n_m < n_1$ [36].

[2] At distances larger than 100 nm the coupling of instantaneous dipoles is weakened by the finite speed of light, however. The effect is known as *retardation* of van der Waals forces [37].

3.2.3 Capillary forces

For SFM measurements made in air, or in general for humid systems, the capillary force can be the strongest interaction between two small bodies. A water bridge, *meniscus*, spontaneously forms between the contacting bodies from ambient humidity, and the surface tension causes a negative Laplace pressure inside the liquid, which pulls the bodies strongly together. A humidity independent approximation [37] can be used for large ($R >1\ \mu m$) sphere on a flat surface:

$$F_{cap} = 4\pi\gamma R\cos\theta, \tag{3.4}$$

where γ is the surface tension and θ is the contact angle between water and surfaces. It can be shown, however, that for smaller particles ($R<1\mu m$) a clear deviation from the basic model is seen, and a strong humidity dependence of the force arises [41], and the force splits into two separate components, as explained in Section 3.7.

3.2.4 Other forces relevant for some SFM systems

The *image force* is due to polarization of a conducting material caused by point charges in another object. The point charges cause an additional potential on the conductors, and this changes the charge distribution on them. These *image charges* then interact with each other and with the point charges [32].

If there is a direct electrical connection between a SFM tip and a surface, both made of conducting material, electrons need to spend energy to cross the barrier from a material of smaller work function to a material with a higher one. This will cause a contact potential U between them, which produces a *capacitance force.*

Magnetic forces are usually important only when both objects are ferromagnetic. It has been suggested [42] that to study atomistic magnetization by SFM, it would be possible to measure the difference in force between spin down and spin-up atoms on the surface with a spin-polarized tip. This difference would directly give the *exchange interaction.* The first experiments to measure this weak difference on antiferromagnetic NiO(001) surface have been performed recently [43].

Charges can accumulate on tip or surface during preparation, cause a additional strong tip-sample interaction, show as artifacts in images, and even prevent stable SFM imaging on many systems. The problem is limited to insulating materials, as there the charges get localized, whereas on conductors free charges would conduct away. In many experiments the tips are made of silicon, onto which a thin silicon oxide layer forms, and can get charged, and often the sample surfaces are prepared by cleaving a crystal, which can cause massive surface charging, making imaging such surfaces, such as MgO or alumina, hard to perform experiments on.

3.3 Simulating SFM imaging

Once we have calculated the tip-sample forces, there are other elements as well, that are needed to model scanning force microscopy. This section will explain how different aspects of modeling, short-range forces, long-range forces, and cantilever dynamics are combined to obtain frequency shift data directly comparable to experiments, and how this data can be used to produce images or scan lines of surface features.

3.3.1 Tip models

As mentioned in the introduction of this chapter, choosing proper tip models for simulation is maybe the most crucial part of modeling SFM. Often the motivation for simulation is to explain features seen in experimental images, therefore the physics of simulation must be in agreement with the experimental system. Often the experiment does not give any straightforward clue of what the very apex of the tip could be, however, and careful planning must be made to cover the possibilities. Especially when modeling atomic resolution details in SFM, the nature of the tip model completely determines the chemical interactions between the tip and the surface, and results can vary strongly between different models.

As the SFM tips used in experiments are usually manufactured from silicon, it is also the most common choice of tip materials in simulations. However, it is too simplistic to assume that the correct model for the tip apex really is bulk silicon, for several reasons:

- In experiments, the silicon cantilevers are transferred into the vacuum chamber from ambient air, and it is well known that this forms a silicon oxide overlayer of a few nanometers in thickness to the tips made of silicon.

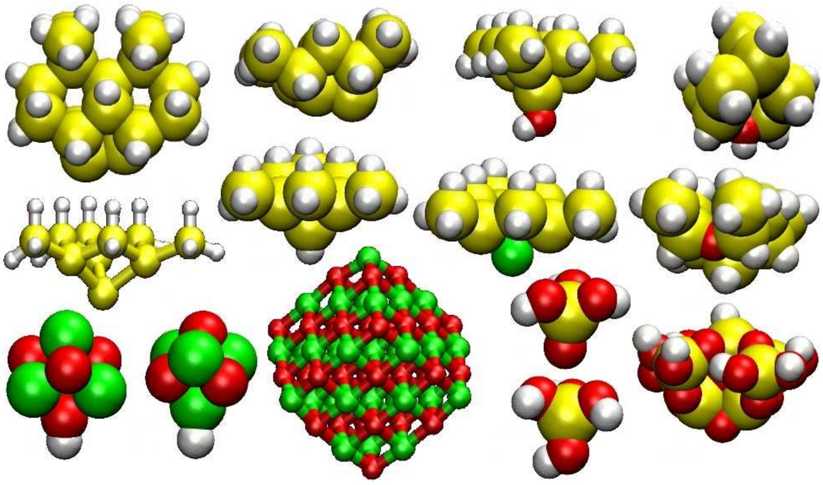

Figure 3.1: *Different tip models to calculate the chemical interaction for atomistic SFM imaging. Silicon atoms are shown in yellow, oxygen red, magnesium green, and hydrogen white.*

- In majority of experiments, there is observable contact between the tip and the sample before the images are obtain, often this enables best contrast. Therefore also the surface materials may form the tip apex.

The atom closest to the imaged surface has the largest impact on the interaction, but the rest of the model is important as well: obviously the bonding characteristics of a isolated atom are very different from those that is positioned to a corner of a cluster. In addition, also the mechanical properties like elasticity of the tip apex strongly affect imaging at atomic resolution, as it determines how easily the apex can bend or stretch to form the strongest bond or towards the weakest repulsion [44].

3.3.2 Cantilever oscillation properties

Cantilever oscillation can be described by the equation of motion [8]:

$$\frac{k}{(2\pi f_0)^2}\ddot{z} + \alpha\dot{z} + kz - F(z+h) = F_{exc}, \tag{3.5}$$

where k is the spring constant of the cantilever, f_0 is the oscillation frequency of a free cantilever ($F_i = 0$), α is the damping constant, h is the equilibrium height of the cantilever form the surface without interactions, F is the tip-sample force, and F_{exc} is the excitation fed to the cantilever to keep the oscillation amplitude constant. At constant amplitude the excitation exactly compensates the damping, and assuming the tip-sample interaction $F(z)$ is time-independent, we can simplify the previous expression to the following form:

$$\frac{k}{(2\pi f_0)^2}\ddot{z} + kz - F(z+h) = 0. \tag{3.6}$$

This conservative equation of motion can be solved by approximating the periodic cantilever movement as a perturbed harmonic oscillator, and the frequency shift can be calculated from [4]:

$$\Delta f(h) = -\frac{f_0}{k} A_0^2 \langle F(z) \rangle. \tag{3.7}$$

By assuming that the tip-surface interaction can be expressed by a single power law $F(z) = -Cz^{-n}$, the frequency shift for the whole oscillation cycle becomes

$$\Delta f = \frac{f_0 C}{2\pi k A_0 d^n} \int_0^{2\pi} \frac{\cos x dx}{\left[1 + (\frac{A_0}{d})(\cos x + 1)\right]^n}, \tag{3.8}$$

where d is the smallest tip-surface separation during the oscillation cycle and $x = f_0 t$. For a more thorough discussion, see for example ref. [8].

3.3.3 Producing simulated SFM images from frequency shift data

Using the procedure explained above, the simulated force field over the surface can be transformed into a map of frequency shift $\Delta f(x, y, z)$ above simulated points. The final step for generating simulated SFM images is to find by interpolation a constant frequency shift surface $z(x, y)|_{\Delta f_c}$, and to plot this topographic image of the surface, or alternatively, plotting the frequency shift at constant height z_0, producing a constant height image $\Delta f(x, y)|_{z_0}$.

Complementary to forming surface images, scan lines can give a more quantitative measure of surface atom corrugations or cluster profiles. Scan line frequency shift data is formed similarly as the data for images, but in this case height z is plotted on the vertical axis as a function of horizontal coordinate x running along the scan line, instead of showing z only as color in $z(x, y)$ images. An experimental example is shown at the bottom of figure 5.2.

3.3.4 Accuracy of SFM simulations

As in all computational physics and most of other science, results of SFM simulations are not exact. On the contrary, there are several sources of error in the path from choosing the simulation system and methods to the final simulated SFM images. Calculation of the tip-sample interaction with a well-selected method and parameters produces results of a good precision, although as this is the most computationally expensive part of the simulation, compromises between accuracy and cost have always to be made. The routines used to convert the interaction into frequency shift are reliable as well. The fact that most of the computational SFM work is very tight co-operation with experiments means that the largest sources of uncertainty are in fact experimental: especially the exact atomic structure of the tip apex, as well as the macroscopic radius of the tip and surface charging, to some degree, are unknown. Especially the former can at worst cause an uncertainty of close to an order of magnitude in the calculated forces, and better tip models need to be tested. This means that theory and experiment are most often not in strictly quantitative agreement, even though a rather good agreement is sometimes found. Often it is, however, the *qualitative* agreement that the research is after, and typical accuracy is enough to explain imaged patterns and explain the experimental findings. In force spectroscopy (Section 2.6) a quantitative comparison is possible, and also the demands for computational accuracy increase.

Calculating tip-surface interactions

3.4 Density functional theory

Density functional theory (DFT) [45, 46] has become the standard tool for *ab initio* materials physics and quantum chemistry during the last decades, because of the good accuracy it provides for a reasonable computational cost. For simulating SFM, density functional theory presents the most practical way to simulate the chemical short-range interactions at the quantum mechanical level, as well as to calculate the material properties of the system simulated. Although the computational cost of even the fastest implementations of DFT is very heavy compared to the semiempirical methods shortly introduced in Section 3.5, systems with representational power, with about one hundred atoms, can be routinely simulated. Commercial and academic packages to solve varying physical problems are available, and in principle can be used with a *black-box approach*, without knowledge of the underlying theoretical foundations of DFT. However, for trustworthy results and performance optimization, the user of the method needs a proper knowledge its details, limitations, failures and different implementations.

3.4.1 Introduction to DFT

The basic assumption for most quantum mechanical calculations of condensed matter is the separation of electronic and ionic degrees of freedom. This is known as the Born-Oppenheimer approximation: movement of atom nuclei is very slow compared to electronic movement, thus the nuclei are considered to form a static external potential V in which the electrons move. These electrons are described by a many-particle wave function $\Psi(\vec{r_i}, ..., \vec{r_N})$, which fulfills the Schrödinger equation for the many-electron system:

$$\hat{H}\Psi = [\hat{T} + \hat{V} + \hat{U}]\Psi = \left(\sum_{i}^{N} \left[-\frac{\hbar^2}{2m}\nabla^2 + v(\vec{r_i}) \right] + \sum_{i<j}^{N} \frac{q^2}{|\vec{r_i} - \vec{r_j}|} \right)\Psi = E\Psi, \qquad (3.9)$$

where $\hat{H}$ is the many-body Hamiltonian, and its components represent the kinetic energy, external potential from the nuclei, and electron-electron interaction, respectively.

While sophisticated approaches to solve this many-body problem exist, they are all computationally very expensive, and therefore suitable only for systems with a small number of electrons. Density functional theory provides an alternative way of calculating the properties of a many-electron system: the many-body problem is mapped into a single-body problem, well tractable to larger system sizes up to thousands of atoms.

Density functional theory stands on two proofs: Hohenberg-Kohn theorems [47] show that the complicated wave-function representation of the electronic system can be replaced by a simpler representation with electronic density $n(r)$:

1. There exists a one-to-one mapping between the electronic ground state density and the ground state wavefunction of a many-electron system: The ground state is a unique functional of the ground state density $\Psi_0 = \Psi_0[n_0]$.

2. The ground state electron density provides the minimal total electronic energy of the system, among all trial densities with the same number of electrons. This is known as the *variational principle*: the ground state density can be found by searching the density $n = n_0$ that minimizes the energy, with the constraint that the integral of density must match the total number of electrons.

Further, the Kohn-Sham ansatz shows that the intractable many-body problem of interacting electrons in a static external potential is reduced to a tractable problem of fictitious non-interacting electrons moving in an effective potential, with the same density [48]:

$$\left[-\frac{\hbar^2}{2m}\nabla^2 + V_s(\vec{r}) \right]\phi_i(\vec{r}) = \varepsilon_i\phi_i(\vec{r}), \qquad (3.10)$$

where the orbitals ϕ_i reproduce the density $n(\vec{r})$ of the original many-body problem:

$$n(\vec{r}) = n_s(\vec{r}) = \sum_{i}^{N} |\phi_i(\vec{r})|^2 . \qquad (3.11)$$

Here the effective potential

$$V_s(\vec{r}) = V_{ext}(\vec{r}) + e^2 \int \frac{n_s(\vec{r}\,')}{|\vec{r} - \vec{r}\,'|} dr' + \frac{\partial E_{xc}[n_s]}{\partial n_s}, \tag{3.12}$$

where the last term, *exchange-correlation potential*, contains all the many-body effects.

As the Hartree- and exchange-correlation parts depend on n_s, which depends on ϕ_i, which again depends on V_s, the solution of the equations must be obtained self-consistently, *i.e.* one starts with an initial guess for density $n(r)$, calculates $V_s(r)$ and solves the Kohn-Sham equation Eq. 3.10, and obtains new density $n(r)$ from the solved ϕ_i, and continues the iteration until convergence is reached.

3.4.2 Approximations: exchange-correlation functionals and pseudopotentials

The Kohn-Sham method presented above is in principle exact, but in practice approximations are needed, as the exact exchange-correlation functional is not known. In the original 1965 paper [48] Kohn and Sham write the exchange-correlation energy for slowly varying density as

$$E_{xc}[n] = \int n(r)\varepsilon_{xc}(n(r))dr, \tag{3.13}$$

where $\varepsilon_{xc}(n(r))$ is the exchange-correlation energy of homogeneous electron gas of density n, which is well known *e.g.* from quantum Monte Carlo calculations [49]. This is the *Local Density Approximation* (LDA). Strictly the functional can only be used for systems with slowly varying density, but it has proven to be surprisingly accurate even for systems that are far from homogeneous, e.g. single atoms.

Although many physical properties are properly calculated by LDA, non-local corrections are often needed for accurate description. The most popular group of improved exchange-correlation functionals is known as the Generalized Gradient Approximation (GGA). In GGA the exchange-correlation energy is a functional of both the density and its gradient, $E_{xc} = E_{xc}[n(r), \nabla n(r)]$. In contrast to LDA, there are several parameterizations to GGA, with slightly different strong areas, PBE [50], PW91 [51] and BLYP [52, 53] are some of most common. Generalized gradient approximations generally (but not always, especially in solids) improve the ground state energies, bond lengths and dissociation energies of molecules, and cohesive properties of solids over

LDA [51], and *e.g.* give the proper ferromagnetic bcc ground state for solid iron [54], which LDA fails to generate.

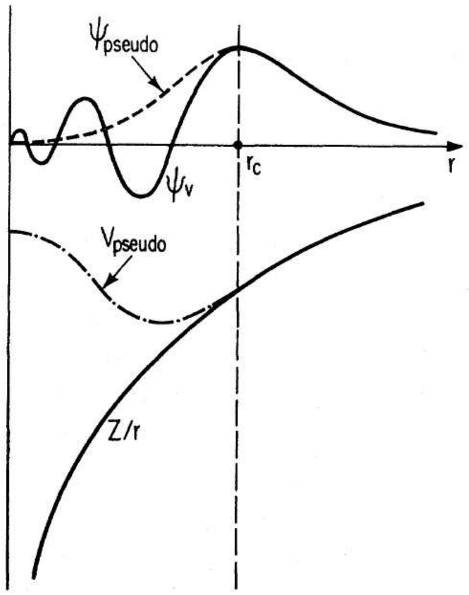

Figure 3.2: *Illustration explaining all-electron potential (solid line) and pseudopotential (dashed line), and the corresponding wavefunctions.* r_c *designates the radius above which the all-electron and pseudopotential values are equal [55].*

Another approximation often used in DFT is the use of *pseudopotentials* [56]. The core electrons of atoms are experiencing a strong Z/r potential, and this combined with orthogonality requirements makes the wavefunctions rapidly oscillating and computationally expensive to model. At the same time, however, the core electrons are only affected very little by the surrounding atomic environment. Therefore in many calculations smooth pseudopotentials are constructed for each element (see figure 3.2), to take into account the effect of nuclei and core electrons, and only the valence electrons are explicitly treated. Pseudopotentials match the true potential outside the core radius r_c.

3.4.3 Tip-sample interactions in DFT

The tip-surface forces can be obtained from the DFT (or other atomistic) calculation by freezing a part of the system, typically the lowest surface layer and the top half or third of the tip atoms, and allowing other nucleic positions in the system to *relax*, utilizing for example the conjugate gradient method [57]. Once the system has relaxed, *i.e.* the sum of forces to each unfrozen nucleus is below a small threshold (e.g. 0.02 eV/Å), the sum of forces to the frozen part of the tip (or the surface) gives the total tip-sample short-range interaction strength.

Forces on ions at positions R_I are given in DFT by the Hellmann-Feynman theory [58, 59]:

$$\frac{dE}{dR_I} = \frac{\partial E}{\partial R_I} = \frac{\partial \langle \psi_i | H | \psi_i \rangle}{\partial R_I} = \langle \psi_i | \frac{\partial H}{\partial R_I} | \psi_i \rangle. \tag{3.14}$$

The expression is only accurate for wavefunctions that are very close to the exact eigenstates of the Hamiltonian, when the electronic degrees of freedom (not shown) give no contribution. When the Hellmann-Feynman forces are calculated with a method using a non-complete basis set (such as LCAO basis explained below), error correction terms for the *Pulay forces* are needed [60].

3.4.4 SIESTA: DFT code for solids

In this work all the DFT calculations have been performed with the SIESTA [61, 62] code, which utilizes a linear combination of numerical atomic orbitals (LCAO) as the basis set, allowing multiple-zeta, polarized orbitals. The code projects electron density and wavefunctions onto a real-space grid to calculate Hartree and exchange-correlation potentials. The generalized gradient approximation (PBE) was used for the exchange-correlation functional, and pseudopotentials were of the fully non-local Kleinman-Bylander form [63].

Compared to a plane-wave basis, for example, the LCAO basis enables faster and larger calculations, mainly due to the strict cutoff at r_c in the basis functions, which increases locality, and enables even linear scaling for large systems. As a disadvantage, the method provides no systematic way to obtain convergence (such as the plane-wave cutoff energy), so that many parameters must be optimised to achieve both reliable results and the needed level of accuracy. In general, to test the accuracy of the computational setup with the selected parameters and generated pseudopotentials, convergence of the total energy, bulk lattice constants and dimer lengths can be calculated for materials studied, for example.

3.5 Atomistic simulations with pair-potentials using MARVIN2

For the simulation of interactions in ionic systems, because the electron charge density is strictly localized onto ions, and charge transfer is non-significant, it is often sufficient to use methods based on classical pair potentials, computationally several orders of magnitude cheaper than DFT. One method is the Shell Model, where atomic polarization is modeled according to the Dick-Overhauser model [64], in which each ion is represented by a core charge Q and a massless shell with charge q, connected by a harmonic spring. The interactions between ion cores and shells are represented by empirical potentials, specifically fitted to match reality for each core-core, core-shell, and shell-shell interaction. The interactions typically include three components: Coulomb electrostatic interactions, van der Waals interactions, and repulsive short-range interactions between the shells.

MARVIN2 [65] program has been used for shell model simulations. Simulations were performed on a periodic surface cell, where long-range Coulomb interaction diverges, if trivially summed between a charge and all the other charges both in the same simulation cell and in all of its periodic images. *Ewald summation* [66], which utilizes the screening of the Coulomb interaction by surrounding ions, is used to calculate the long range contribution to the total energy.

3.6 Volume element code for van der Waals interactions

To model the van der Waals forces in many applications, analytical formulae for the interaction are often used. The additivity of the interaction makes writing such expressions simple, but it also allows novel computational models to be built, which can tackle problems where ideal geometries of analytical expressions are not enough. As the interaction is additive, it is possible to build a computational model where arbitrarily shaped objects can be built from thin, vertical, cuboidal volume elements, and the interaction is summed between each volume element pair [67]. This results in a four-dimensional (discrete) sum, which can in our application size (up to 500×500 grid points) be computed in a few minutes on a single personal computer. Usually the full calculation of a force field includes hundreds or thousands of these single-point force calculations, resulting in a calculation time of a few days.

The van der Waals interaction for two infinitesimal volume elements, shown in equation 3.2, can be integrated for two aforementioned vertical volume elements:

$$\begin{aligned} F_v &= \frac{A^2 H}{8\pi^2 dr^5}\Bigg[\frac{dr(5dr^2+3(k-z_1)^2)(k-z_1)}{(dr^2+(k-z_1)^2)^2} - \frac{dr(5dr^2+3(k-z_2)^2)(k-z_2)}{(dr^2+(k-z_2)^2)^2} \\ &\quad -3\arctan(\frac{z_1-k}{dr}) + 3\arctan(\frac{z_2-k}{dr})\Bigg], \end{aligned} \tag{3.15}$$

where A is the horizontal cross-section area of the volume element, H is the Hamaker constant of the materials[3] (defined in Eq. 3.3), dr is the horizontal separation of the volume elements, k is the height of the upper end of surface volume element (lower end at $-\infty$), and z_1 and z_2 are the heights of the lower and upper ends of tip volume elements, respectively.

As the simulation is utilizing a discrete grid to represent the interacting bodies, the results suffer from a discretization error. The model includes further correction terms for the horizontal separation parameter dr, which kept the discretization error below 3 % in all calculations, well below the error caused by other uncertainties of calculations (e.g. actual tip shapes, exact experimental cantilever oscillation parameters.) The complex (and unintuitive) correction terms are not presented here.

3.7 Simulating capillary forces

Interactions between surfaces vary depending not only on their properties, but also the environment. In a humid ambient, like air, water condenses from the ambient to form water films on surfaces, and bridges between two surfaces near contact. This water *meniscus* causes a usually attractive interaction between the surfaces or particles, and often becomes the dominant interaction in this environment. Capillary forces between macroscopic (> 1 μm) objects are rather well known, and can be dealt with simple approximations [37]. At the nanoscale, however, where the typical diameter of the interacting object (for example a SFM tip, $r \approx 10$ nm) is comparable to the effective radii of these menisci, the approximations valid for large length scales no longer work, and recently the interest in the properties of these systems has been revived. Modeling of capillary forces was studied in Publication **II**, concentrating mainly on the application of scanning force microscopy on adhesion measurements in a humid ambient. The following treatment is applicable for length scales where continuum theories are applicable, properties of capillary menisci are determined by the competition of interfacial energies, and the actual molecular structure of water is still not needed.

---

[3] Hamaker constant between two different materials in vacuum is given by $H_{12} \approx \sqrt{H_1 H_2}$

3.7.1 Introduction to capillary forces

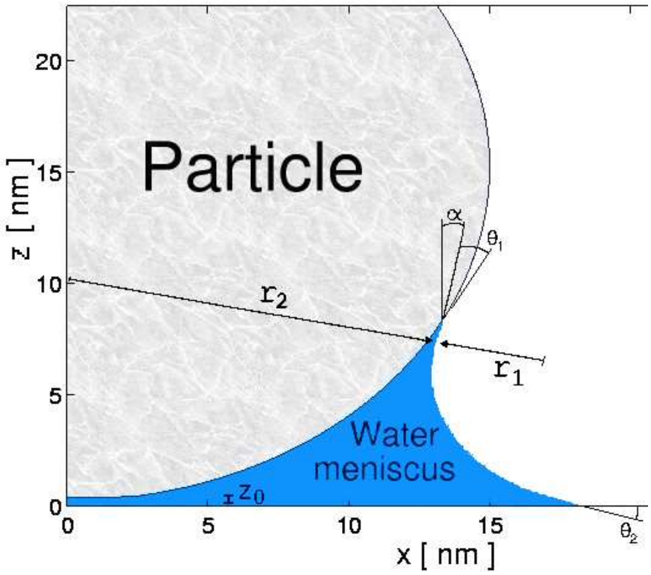

Figure 3.3: *Meniscus profile can be numerically calculated for a tip-sample system. The two principal radii r_1 and r_2 are obtained from the Kelvin equation (Eq. 3.16).*

To model capillary forces, and test the applicability of the simple approximation often used, another numerical model was built. In the following text the model system is assumed to contain a flat surface and a particle/SFM tip in contact. For simplicity, the model geometry is axially symmetric, but otherwise it is calculating the exact geometry-specific solution (side profile is nodoid [68]) of the Kelvin equation [69]:

$$r = \frac{\gamma v_0}{k_B T \ln H_r}, \tag{3.16}$$

for total curvature r of the meniscus surface, where γ is the surface tension, v_0 is the molecular volume of the liquid, k_B is the Boltzmann constant, T is system temperature and H_r is the relative humidity. Due to this negative total curvature of the concave meniscus (see figure 3.3), the surface tension γ causes a large pressure difference between the ambient and the meniscus liquid, known as Laplace pressure:

$$\Delta p = \gamma / r. \tag{3.17}$$

This negative pressure in the liquid, in combination with a direct surface tension component, causes an attractive force between the surfaces limiting the meniscus.

The most common approximation to make in calculating capillary forces is to assume that the vertical dimension of the meniscus is negligible compared to horizontal dimensions, and therefore the smaller dimension completely defines the meniscus curvature pressure. This allows the simple approximation of Eq. 3.4 to be formulated, if the particle shape is approximated spherical. Utilizing the fact that for a sphere, the area covered by the meniscus (growing with increasing relative humidity) increases as $A \propto r_{xy}^2 = (r_z^{\frac{1}{2}})^2 = r_z$ whereas the capillary pressure drops as $p \propto r_z^{-1}$, we can formulate $F = pA \propto r_z r_z^{-1}$ *i.e.* the force is humidity independent. This most surprising result (after all, capillary forces are caused by condensing water into a meniscus, strongly dependent on relative humidity) has obvious limitations. The condition that the vertical dimension of the meniscus is negligibly small was shown to be true for objects in the micrometer range and above, but to fail for objects of size below a micrometer [41], matching with experiments [70, 71].

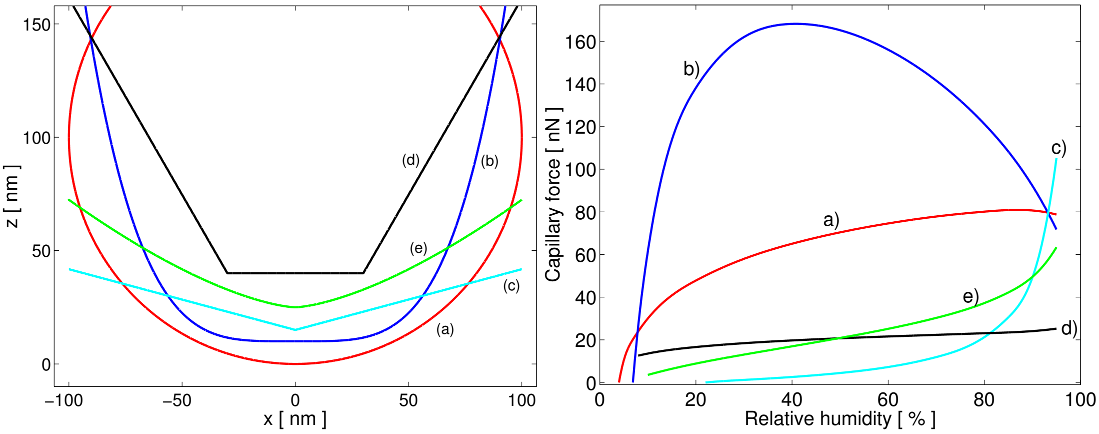

Figure 3.4: *(Left) Tip profiles used to calculate capillary forces. (Right) Capillary forces for the corresponding tip shapes. There is certainly a clear variation from the basic approximation, Eq. 3.4, which predicts a humidity independent force of 91.5 nN.*

Figure 3.4 shows the dependence of humidity for the capillary force (right), calculated for several different particle shapes (left) of roughly the same dimensions as a 100 nm radius sphere. The humidity dependence is strong for most of the shapes of this size, and also the deviation between different shapes is very clear – therefore the applicability of approximating the force with a humidity independent result of 91.5 nN given by Eq. 3.4 for a spherical particle is very questionable.

In macroscopic approximations typically only the capillary pressure component is treated, and the direct surface tension component of the capillary forces is neglected as small. This was shown to be a valid approximation for large objects, but again fails at the nanoscale. As shown in figure 3.5, for spherical particles of radius above 100 nm, the surface tension component remains below 10 % of the total capillary force, whereas for 15 nm radius it becomes equal to the pressure component at high relative humidity. In systems this small, however, limits of continuum modeling may change real behavior in either direction.

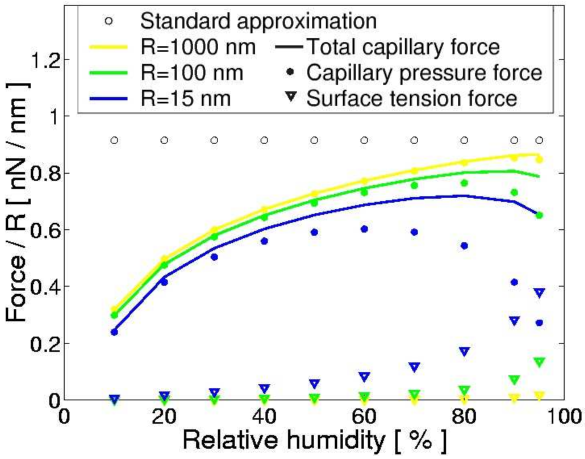

Figure 3.5: *Capillary force components (pressure and surface tension) shown for different spherical particles on a flat surface. The capillary pressure force dominates the interaction, except for small particles at high humidity.*

Another linked approximation is to assume that the side profile of the capillary meniscus is an arc of a circle. It is based on the presumption that the curvature of the side profile is constant, which is only true if the vertical dimension of the meniscus is negligible compared to horizontal dimensions. Comparison between the true nodoid solution of the Kelvin equation and an arc of a circle showed that the approximation is valid for all length scales where the continuum modeling can be assumed to be applicable, with errors well below 5 % even for 15 nm radius particles.

Approximations to the capillary force also predict another deviation from the nanoscale experiments: in simple approximations the capillary forces have a finite (nearly constant) value in the limit of zero humidity, as the magnitude of the negative Laplace pressure increases with decreasing humidity and meniscus volume, $\lim_{H_r \to 0} \Delta p(H_r) = -\infty$. Experiments show instead a threshold of about 20-40 % of relative humidity, below which the capillary forces are negligible. This discrepancy is typically explained by a finite gap (even less than 1 nm) between the surface and the "average perimeter" of the adhered particle, caused by small roughness in both objects [41, 71]. There are other possible explanations as well: The continuum models assume that the magnitude of the negative Laplace pressure can increase without limit, but this assumption fails as all material have a finite tensile strength. For water the estimated theoretical tensile strength is between -500 and -3000 bar [72], experimentally -1400 bar has been reached [73]. If applied to the calculation of maximum Laplace pressure Δp_{max} in a water meniscus, these values correspond to a threshold humidity H_{min} of 69 %, 11 % and 35 %, respectively, via expression

$$H_{min} = \exp(\Delta p_{max} v_0 / k_B T). \tag{3.18}$$

The upper theoretical value and the experimentally measured value correspond well to the threshold in capillary force experiments. In macroscopic samples, already at clearly lower tensions, the negative pressure is released by cavitation (formation of bubbles), but the critical radius for these is on the order of 100 nm [72], thus the effect is absent at the nanoscale.

The observed behavior at low relative humidity can also be seen as a failure of continuum modeling approach to correctly represent the formation and properties of a capillary meniscus of very small dimensions. At this limit the actual molecular structure effects, like solvation forces caused by the layering of confined water [37], cause simple continuum concepts like surface tension to lose their capability to describe the physics of a water meniscus.

3.7.2 Numerical method

In our model the side profile of the capillary meniscus is built from very short line elements, arranged consecutively to form the profile in such a way, that at each point of the curve the total curvature radius matches the constraint given by the Kelvin equation, thus the profile is non-circular. The total curvature set by Eq. 3.16 can be split into two components, namely the two principal radii of curvature (see Figure 3.3):

$$r = (\frac{1}{r_1} + \frac{1}{r_2})^{-1}. \tag{3.19}$$

The first line element touching the tip surface is set to the proper contact angle θ_1 determined by properties of the material. The end point of this line element now determines the local horizontal curvature radius r_2, and consequently the proper vertical curvature radius r_1 can be obtained from equations 3.16 and 3.19. The radius of curvature can be calculated as

$$r_1 = \frac{[1 + (dx/dz)^2]^{\frac{3}{2}}}{d^2x/dz^2}, \tag{3.20}$$

from which we can solve the direction of the next line element:

$$\frac{d^2x}{dz^2} = \frac{[1 + (dx/dz)^2]^{\frac{3}{2}}}{r_1}. \tag{3.21}$$

This arranging of line elements is continued until the sample surface is met, and the calculations are iterated until the profile meets the surface at the correct contact angle θ_2.

3.7.3 Conclusions

The model created to simulate the capillary phenomena numerically can be used to calculate the meniscus profiles and capillary forces for any axially symmetric systems, and therefore a much more thorough comparison between experiment and theory is made possible – for example, the meniscus shapes for SFM tip profiles obtained directly from experimental inverse SFM measurements can be used, instead of simple idealized shapes. Applied to different configurations relevant for SFM application in a humid ambient, the results of the model have helped to evaluate the applicability of approximations, and to systematically examine the dependence of capillary forces on different parameters of the system.

Chapter 4

Simulating atomic resolution SFM imaging

Maybe the most intriguing promise of scanning force microscopy has been its ability to *see* atoms on surfaces. A true atomic contrast allows scientists to see the exact organisation of surface atoms, different surface reconstructions, and atomic defects on the surfaces, as well as to study adsorbates or clusters on surfaces in atomic detail. Clear atomic resolution is also a prerequisite for atomic manipulation experiments. The output of the actual instrument is, however, only a two-dimensional image with patterns which need interpretation, and this final step before a scientific result is often the most difficult. As the detailed atomic structure of the SFM tip apex determines the contrast pattern obtained, interpretation of images from surfaces composed of several elements, even the simple cubic crystals such as NaCl and MgO, requires either a solid determination of the tip apex composition or use of markers, such as defects, helping to determine atomic species on the surface. As the control of tip apex composition is in general experimentally inaccessible, only a comparison with numerical SFM simulations, where information of atomic composition is naturally available, can provide a reliable interpretation.

Atomic resolution SFM imaging of titanium dioxide (110) surface was studied in Publication **I** utilizing both first-principles and atomistic methods. Publication **IV** presents simulating imaging of a potassium bromide surface, KBr (001) by first-principles methods, studied in a close collaboration with experimental work by C. Barth and C. R. Henry at CRMCN-CRNS, Marseille, France.

4.1 TiO_2(110) studied with atomistic potentials

Titanium dioxide (TiO_2 or titania) is an important material for many different applications, from biomedical implants to photocatalysts and self-cleaning windows. The surface properties and defects of TiO_2 determine its success in many of these applications, and thus it has been studied in a wide variety of surface studies. TiO_2 occurs in different forms, *rutile* being the most common is discussed here. The most stable surface of this transition-metal oxide is (110). Figure 4.1 shows the atomic structure of the surface, characterized by rows of bridging oxygen atoms over titanium ions [74]. SFM imaging of both the ideal surface and oxygen vacancies on the surface were simulated, to establish a reliable understanding of contrast formation, obtained previously for STM, but lacking for SFM.

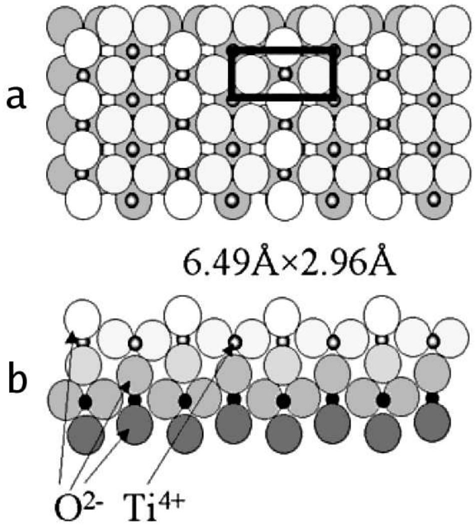

Figure 4.1: *TiO_2(110) surface structure, from (a) top and (b) from the side [75].*

Typical tip models were used for simulation: a ten-atom silicon tip with a dangling bond pointing towards the surface represents a covalently bonding tip, whereas a 64-atom MgO cube, oriented either with an Mg or O atom corner towards the surface, represents an ionic bond. The TiO_2 (110) surface was modeled by a (6×6×3) slab in the atomistic calculations, and by a (4×2×3) slab in the DFT calculations, in terms of the six-atom unit cell of the surface. In both cases the bottom third of the surface atoms, and top third (atomistic) and top half (DFT) of the tip atoms were fixed to their equilibrium positions, and rest of the atoms were allowed to relax freely.

DFT simulations with the SIESTA code (Si tip) and shell model simulations with the MARVIN2 code (oxide tips) produced force curves over different surface sites of the ideal

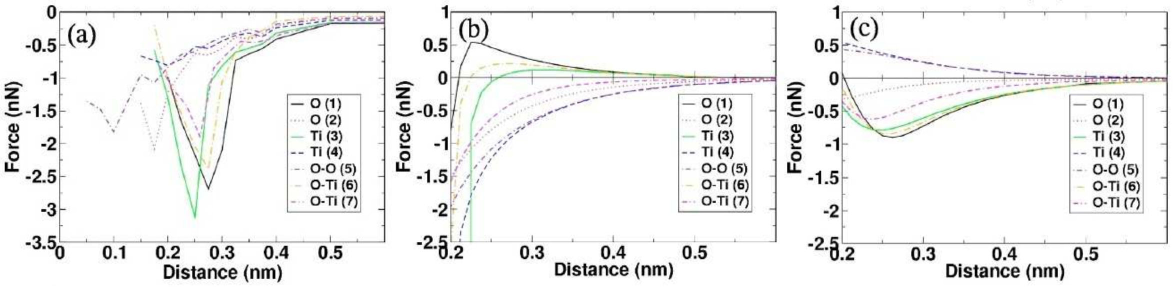

Figure 4.2: *Tip-surface force curves over different sites of TiO_2(110) surface, with three different tip models: (a) silicon tip, (b) oxide tip with oxygen at the apex, and (c) oxide tip with magnesium at the apex [74].*

TiO_2 surface (see figure 4.2.) Calculating the simulated SFM topography images on several frequency shift values, based on this force-distance data, showed that agreement with most experiments on the surface is obtained with a silicon tip or an oxide tip with Mg at the apex (figures 4.3 (a-c) and (g-i), respectively), producing images with bridging oxygen ions shown as bright protrusions. Changes in the electronic structure in the DFT calculations showed a clear onset of covalent bonding (charge transfer of 0.4 electrons) between the Si tip and surface oxygen ions. On the other hand, the third tip (figure 4.3 (d-f)) produced an opposite contrast, showing lower Ti rows as bright protrusions, a pattern also seen in some SFM experiments. This illustrates how misleading the intuitive picture of SFM as a measure of surface geometry can be: the physical corrugation of surface atoms can be inverted in SFM images, depending on tip apex structure.

To cure this ambiguity, further efforts to keep the tip apex free of impurities were proposed, as with a known apex the images can most reliably be interpreted [76]. Simulations of a bridging oxygen vacancy, done with the silicon tip, showed that the interaction with the vacancy is very weak, and the corresponding image would show the vacancies as dark spots on the bright bridging oxygen rows. The surface sites were later unambiguously determined by utilizing water molecules adsorbing onto O-vacancies as markers [77].

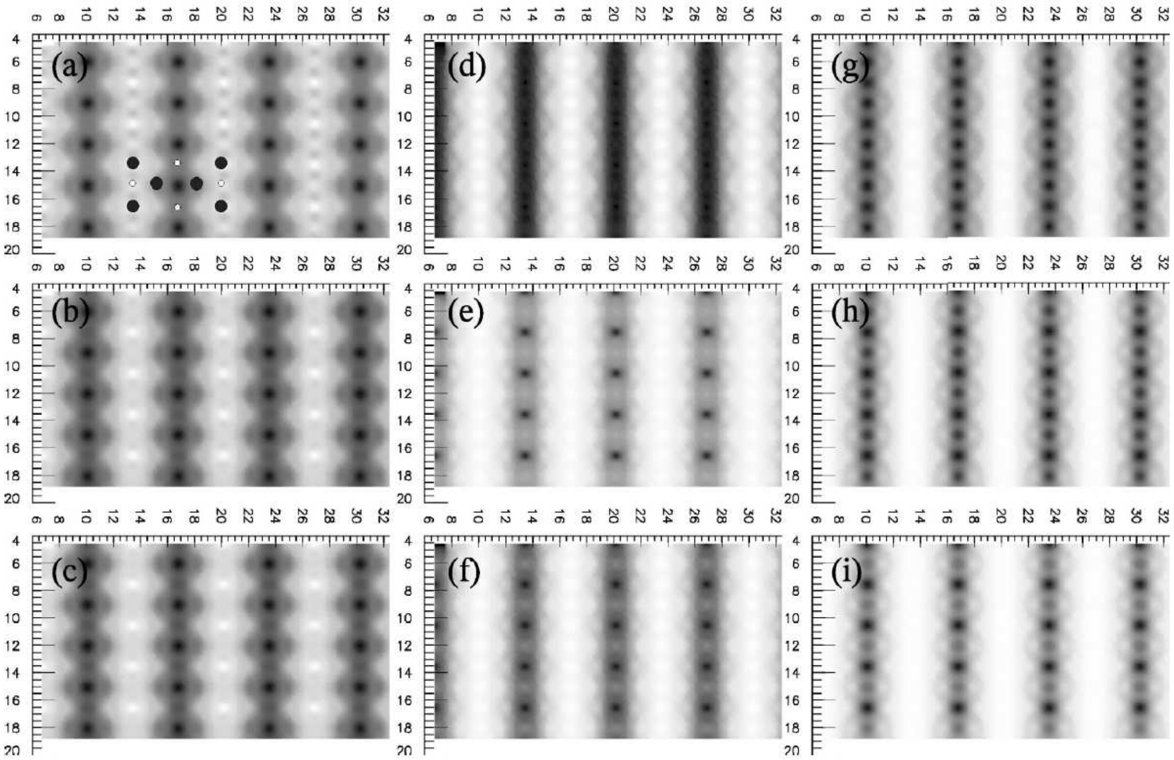

Figure 4.3: *Simulated SFM images of TiO_2(110) surface, (a-c) silicon tip, (d-f) oxide tip with oxygen at the apex, and (g-i) oxide tip with magnesium at the apex. Images were calculated at constant frequency shift of -80 Hz (a,d,g), -90 Hz (b,e,h), and -100 Hz (c,f,i). [74].*

4.2 KBr(001) surface studied with density functional theory

In recent years, the study of small metal nanoclusters adsorbed onto single oxide surfaces has been very active [15, 78]. Although these model systems are not close to the real industrial heterogeneous catalysis systems, they can provide insight to the atomistic reactions of the process. Nanoclustered gold has obtained especial interest, as it shows strong activity in catalysing CO into CO_2 very effectively even at low temperatures [79–85], an application important for car exhaust catalytic converters. Scanning force microscopy provides an effective tool to study these systems, as in principle it is capable of three-dimensional, atomic resolution images both on the metal clusters and on the insulating substrate.

In a previous experimental study [86], gold nanoclusters of less than 10 nm in size were imaged by SFM on a KBr(001) surface. This insulating surface was chosen as it is experimentally easy to prepare and to image in atomic resolution, in comparison to more realistic model catalyst substrates like MgO. The surface was indeed imaged with a clear atomic resolution (see figure 4.4 a.) On the other hand, the gold lacked atomic resolution or even a good contrast on their shape.

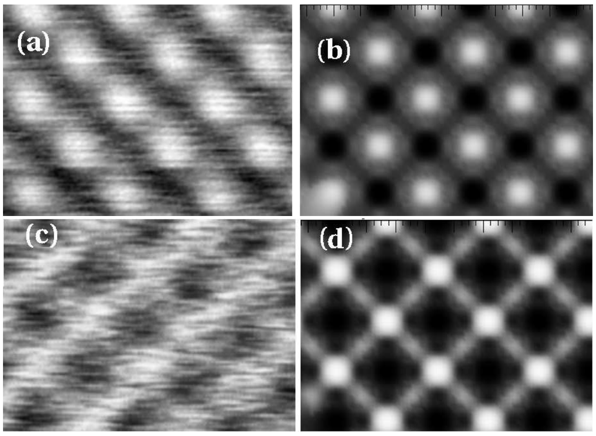

Figure 4.4: *Experimental (a and c) and simulated (b and d) images of the KBr(001) surface. DFT simulations produced distinct surface patterns for different tip apex terminations, (b)* K^+ *ion at the apex, (d)* Br^- *at the apex. Similar patterns were also found in experiment, where the tip termination is unknown. [87]*

In an effort to understand imaging of a system of gold nanoclusters on the KBr(001) surface, the ideal surface was first simulated. The experimental system involving gold clusters set gold also a possible material on the tip apex, and as the atomic resolution experimental images were obtained after contacts to the surface, possible tip terminations for the simulation we chosen as surface materials K, Br and Au.

The choice of these materials, and the following study of gold nanoclusters also fixed our computational method: classical potentials can not be expected to treat interaction with gold atoms properly, let alone electronic structure effects like charge transfer between the surface and the metal nanoclusters, which was also to be investigated. Therefore all the simulations were performed with the SIESTA code, which implements density functional theory. Gold is a very heavy element, and therefore relativistic effects have to be included to the calculation in the form of scalar-relativistic corrections in the pseudopotentials.

In the simulation, the KBr(001) surface was represented by a four-layer slab, where the lowest atomic layer was frozen. To separate periodic images of the tips, 4×4 surface size was found to be enough. Three tip models were used to simulate imaging: K^+- and Br^--terminated $(KBr)_6$ tips (3×2×2 cuboids), seen in the left panel of figure 4.5, and an almost spherical Au_{13} minimum energy cluster [88]. The highest 5 or 6 atoms of the tips were frozen, and the rest of the system was allowed to relax.

The simulated images of the surface match well with the experimental images, K^+-terminated tip model providing the surface pattern (figure 4.4 b) most similar to most of the experimental images (example in figure 4.4 a.) This would identify the bright spots in the images as Br^- ions, and the dark spots as K^+ ions. The species identification from image patterns is not absolutely reliable on this very symmetric surface, but the result matches to that of an earlier force spectroscopy study by semiempirical potentials [89]. Some of the experimental images (figure 4.4 c) look more like the pattern obtained with the Br^--terminated tip (figure 4.4 d). With the Au_{13} tip the pattern was close to the image obtained with the K^+-terminated tip. Both in the experimental and simulated images, the patterns corresponding to the K^+-terminated tip can be mapped into the patterns of the Br^--terminated tip and vice versa by a simple color inversion with little change. The surface patterns are therefore somehow symmetric, even though the change of tip polarity does not produce identical images, as might be intuitively assumed.

4.3 Imaging gold nanoclusters on KBr(001)

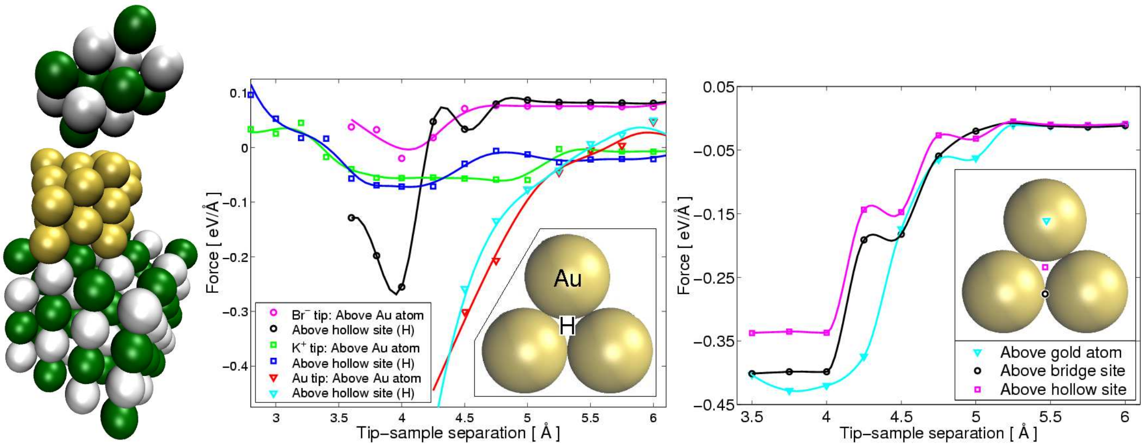

Figure 4.5: *(Left) KBr tip imaging* Au_{25} *cluster on KBr(001) surface. (Center) Tip-cluster forces for* Br^-*-,* K^+*-, and Au-terminated tips. Curves corresponding to* Br^- *are raised by 0.1 eV/Å for clarity. (Right) Forces for a* Br^- *terminated tip imaging Au(001) surface, representing a large cluster.*

To understand the lack of atomic resolution on gold nanoclusters in the experiment, imaging over the clusters was studied computationally. As in the experiments the clusters were 2-15 nm in size, even the smallest were outside the range of reasonable computational capabilities with DFT. Therefore a smaller Au_{25} model cluster (shown in figure 4.5, left panel), providing a relatively flat top facet to mimic larger clusters, was used in the simulation (the cluster was based on a 26-atom 10-8 potential Sutton-Chen cluster [88]). The three $(KBr)_6$ and Au_{13} tips introduced in the previous section were used. The DFT simulations on this small gold nanocluster revealed that with all the tip models there is very little contrast between different surface sites of gold, except for a Br^--terminated KBr tip, where the whole cluster jumped towards the tip, and therefore this would not allow stable experimental imaging (see figure 4.5 center). Similar stability problems were encountered with the Au_{13} tip, due to very strong interaction between the tip and the cluster and high gold atom mobility, whereas the K^+-terminated KBr tip was almost inert. The relaxation of gold atoms in a small cluster is energetically easy both because of the "soft" elastic parameters of gold in general, and because of the low coordination of atoms and the lack of strict crystal order in the small cluster.

As the mobility of atoms in the small cluster was effectively disturbing imaging, another set of DFT simulations was performed with the Br^--terminated KBr tip on the Au(001) (1×5) surface[1] , represented a larger cluster, as a cluster of a size similar to experimental clusters (∼5-10 nm) is clearly computationally too expensive. The Au(001) (1×5) surface presents a much more stable surface for imaging, as all atoms are in plane, and firmly bound to their lattice sites. As shown in the force curves of the right panel of figure 4.5, the potential surface Au(001) presents to the imaging tip is very flat. Obtaining measurable contrast between surface sites is therefore rather difficult also on this densely packed surface or on the clusters it represents, but an estimated contrast of 25 pm may be obtained between the gold atom site and the hollow site in careful experiments, largely due to 24 pm rise of the gold atom when the tip is directly above it. These tiny atomic movements often play a large role in imaged corrugation of surface atoms. The stepped form of the force curves shows these small relaxations of the gold atoms as steep drops in the curve, whereas relaxation of the KBr tip atoms is very small. The flatness of the potential surface of the tip imaging the Au(001) terrace is understandable from the intuitive picture of Au surface: in contrast to distinctive ions of an ionic crystal such as KBr(001), the metal surface has a "sea" of electrons forming a very flat surface to image.

---

[1] The top layer of the surface has a (1×5) hexagonal packing reconstruction, ordered like unreconstructed Au(111) surface, which itself orders in the well-known herringbone reconstruction below 1250 K [90].

Chapter 5

Tip convolution in nanocluster imaging

As seen in the previous chapter for gold nanoclusters, SFM is not capable of atomic resolution in all cases even with the best experimental expertise, and even the shape of three-dimensional objects such as clusters of a few nanometers in size can be very hard to image. This is a remarkable weakness for an instrument that in principle promises to help in building and characterizing tiny structures for nanoscience and nanotechnology.

As explained in Section 2.4, tip convolution can ruin the image quality of clusters small enough. In Publications **III** and **V** the imaging of metal nanoclusters on flat substrates is further introduced, the effects of tip convolution are explained in detail, both from experimental and computational point of view, and the constant height mode of SFM is introduced in this context as a novel way to minimize the effect of the tip on imaging.

5.1 Gold nanoclusters on KBr(001) and HOPG

To understand why the experimental images were of such low quality above the gold clusters [86], in Publication **III** we performed calculations with the numerical continuum van der Waals model explained in Section 3.6, trying to find out the effect of tip convolution to the imaging. During the work it was found that when imaging nanoclusters in constant height mode instead of the more typical topographic mode, image resolution on the top facets of the clusters is increased significantly.

Figure 5.1 shows images of a nanocluster, simulated with three different, simple tip models, both in topographic (left) and constant height (center) mode. Topographic

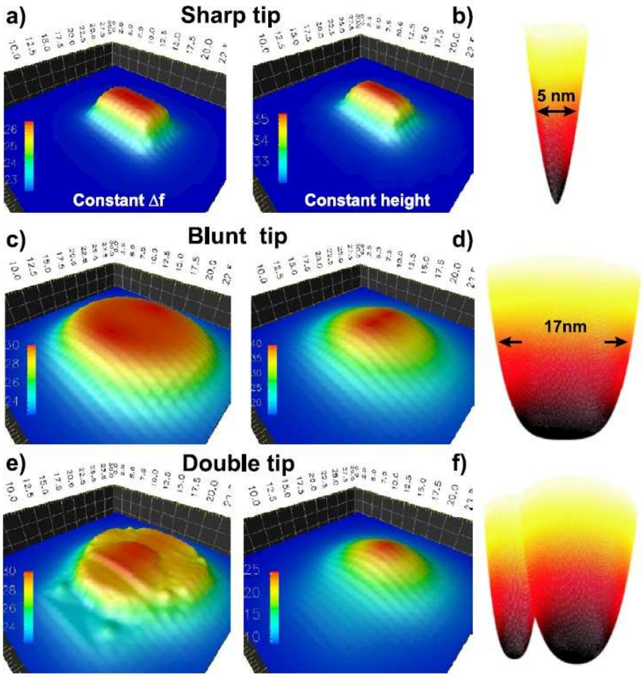

Figure 5.1: *Simulated SFM images of nanoscale clusters on HOPG surface, (left) in topographic mode and (center) in constant height mode, imaged with three tip models (right). Constant height mode greatly improves the imaging quality, largely removing problems seen in topographic mode, (c) from tip bluntness, and (e) tip asymmetry.*

mode image quality depends strongly on sharpness of the tip, as well as its asymmetries, whereas in constant height mode the real dimensions of the cluster are shown more accurately, also on the less ideal tip models. Further, the the effect of the secondary apex in the asymmetric tip was removed.

This difference between imaging contrast of the two modes was confirmed by experiment, which showed even a larger advantage of using the constant height mode in imaging than anticipated by the early simulation results [91]. Figure 5.2 shows an example of experimental images of the same gold nanoclusters imaged in the (a) topographic mode and (b) constant height mode. The shape and size of the top facet of the cluster are clearly more sharply depicted in the constant height mode image, and it is clear that tip convolution softens the details of the topographic image. The line profiles in the image can be used to define a diameter of the cluster, in the constant height mode this is a clearly more well-defined quantity, as the frequency shift curve is much less rounded at the cluster edges than the topographic signal.

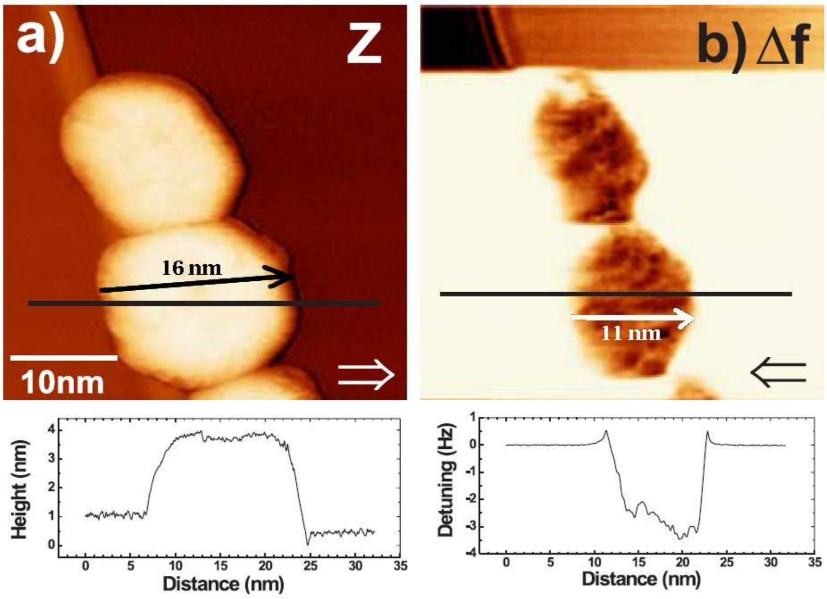

Figure 5.2: *Experimental SFM images of gold nanoclusters on HOPG surface, (a) in topographic mode and (b) in constant height mode. Both the shape and size of the same clusters on surface are seen with much more accuracy in the constant height mode (b). Profiles taken at positions of the horizontal black lines seen below.*

5.2 Pd nanoclusters on MgO(001)

A more relevant system for applications, Pd nanoclusters on the MgO(001) surface, was studied both experimentally and computationally in Publication **V** to understand and improve the image contrast, and to explain the discovered success of constant height mode SFM in imaging nanoclusters.

Our initial hypothesis based on the results of Publication **III** was that the enhanced contrast can only be explained by *i*) a very sharp *nanotip* at the tip apex, and/or *ii*) a short-range chemical interaction between the tip and the sample, forming the sharp image. It was shown, however, that van der Waals interaction alone, with a realistically sharp, asymmetric tip shown in figure 5.4, provides the best match to experiment. Figure 5.3 shows the experimental (a and b) and computational (e and f) results, obtained in topographic (a and e) and in constant height mode (b and f).

The Pd/Mgo(001) system is one of the most important model catalysts [15], and has been frequently studied. Palladium forms clusters sized roughly 5-10 nm in lateral dimensions, and 4-6 nm in height, and their equilibrium shapes are truncated octahedrons [92, 93], when deposited on MgO(001) surface at high temperature in UHV. In

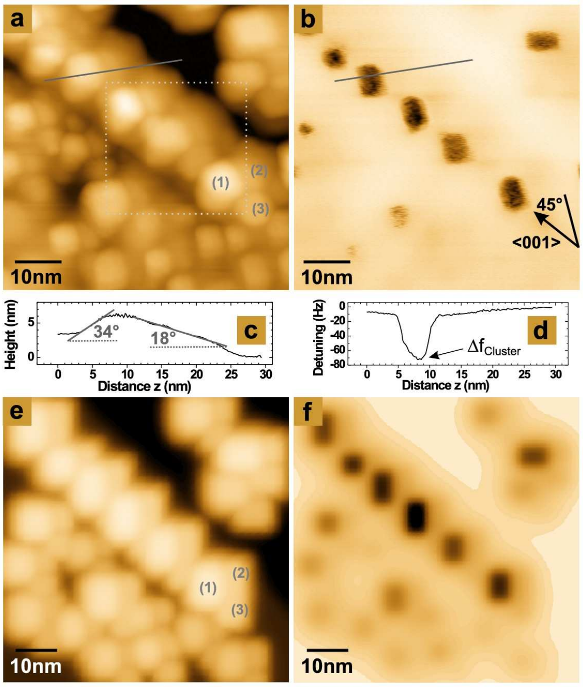

Figure 5.3: *Experimental (a and b) and computational (e and f) SFM images of Pd nanoclusters on MgO(001) surface. Images are obtained in topographic (a and e) or constant height mode (b and f.) Profiles (c and d) are experimental profiles from the grey lines in (a) and (b).*

scanning force microscopy the flat top facets appear rectangular (see figure 5.3), and the accurate dimensions of the clusters can be obtained from top facet dimensions and height.

With the usual topographic mode of the SFM one obtains the cluster heights rather reliably, but tip convolution softens the image enough to render lateral dimensions very inaccurate. Further, as shown by indices 1-3 in figures 5.3 (a) and (e), the topographic mode shows two smaller satellite images for each cluster. As all clusters are shown in a similar arrangement of three apparent clusters, with similar height differences, it is clear that the arrangement is not a feature of the surface, but of an asymmetric tip with side apexes slightly above the main apex.

In constant height imaging mode, on the other hand, height information is lacking, but the top facet dimensions can be accurately measured as edges of the cluster are sharply depicted. Only a single image is obtained for each cluster, and because of the nature of the mode, the clusters lowest in height are not seen in the image at all. Therefore only the combination of the two imaging modes provides the cluster dimensions accurately.

5.3 Explaining the success of constant height mode

The reason for constant height mode's ability to obtain sharper images of clusters on surfaces is not intuitively clear. On the contrary, it is natural to think that for imaging three-dimensional details, the topographic mode following the surface geometry would be ideal. However, in the constant height mode we can use the short-ranged nature of tip-surface interaction to our advantage, even if the SFM tip is not sharp enough to image the surface accurately in the topographic mode. As mentioned in Section 2.4, if the characteristic tip radius r_{tip} is clearly smaller than the dimensions of the surface features d_{surf}, topographic mode works well, but when imaging nanoclusters with a size of a few nanometers, $r_{tip} \approx d_{surf}$, and tip convolution ruins the accuracy of images.

The difference between the two modes is the following: In topographic mode the height signal of the tip, imaging a sharp-edged cluster, follows the tip profile linearly when rounding the cluster corners, whereas in constant height mode the measurement signal, tip-surface interaction, depends stronger than linearly on the separation between the cluster surface and the part of the tip above it, and therefore a stronger than linear dependence on the tip profile is seen, roughly estimating between r^{-2} and r^{-3} even with only rather long-ranged van der Waals forces acting. When imaging is close enough to contain a component of chemical interactions, the distance dependence is strengthened all the more.

The emphasis on the short-range interactions leads to a further advantage in constant mode imaging: the sharpness of images of three-dimensional surface features is less dependent on mesoscopic size and shape of the tip, but is mostly determined by the sharpness of the final nanometer of the tip apex.

Figure 5.4 shows the effect of imaging modes for different tip models, (a) sharp tip, (b) blunt tip with sharp *nanotips* (similar in shape as the tip (a) apex), (c) blunt tip with a chemical interaction. All the tip models have similar side apexes with 2 nm radius at 0.8 nm and 0.9 nm higher than the main apex. For the sharp tip (a), the main apex is paraboloid with 5 nm radius. For the blunt tip (b), the lowest 1.5 nm is the same as on the sharp tip, but above that the profile is a blunter $z \propto x^4$ shape. For the chemically sharp tip, the main apex is a paraboloid with a 25 nm radius, and an additional short-range chemical interaction is operating between the central volume element of the apex and the surface. The short-range potential is based on following

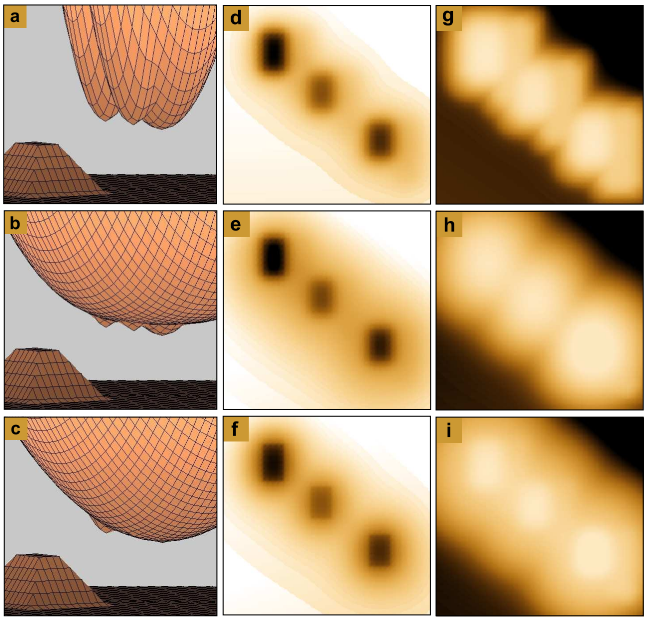

Figure 5.4: *Simulated images of three surface clusters with three tip models:* sharp tip *(a),* nanotip model *(b), and* chemically sharp tip *(c), using constant height mode (d-f) and topographic mode (g-i). See text for details.*

TB-SMA type of a potential [94]:

$$V = Ae^{-p(\frac{r_{ij}}{r_0}-1)} - \xi\sqrt{e^{-2q(\frac{r_{ij}}{r_0}-1)}}, \tag{5.1}$$

where A =7.38 meV, p =6.40, ξ =169 meV, q =1.75 and r_0 =0.3018 nm. This generic example of the chemical interaction remains below 30 % of the total interaction strength.

Constant height mode images (d-f) are very similar for all tip models, as the very end of the tip is effectively sharp for all of them, but the topographic mode images (g-i) differ considerably - only the sharp tip (a) shows some detail on the cluster size and shape, as other tips are too blunt, and the images show mainly the tip shape, due to tip convolution. The side apexes of the tip show only in the topographic mode image for the sharp tip. These results show how the constant height mode greatly enhances the effect of the sharpness of the last nanometer of the tip apex, and details of the tip above that do not show in images, whereas in the topographic mode both the bluntness of the tip and side apexes (or asymmetric tip shape) ruin the image quality.

Chapter 6

Conclusions and outlook

This thesis presents methods and results for numerical simulation of dynamic scanning force microscopy (SFM), focusing on flat surfaces as well as nanoclusters, in UHV conditions as well as in a humid ambient. Scanning force microscopy has become one of the leading methods to image, analyze and manipulate atomic scale structures and surfaces, and promises to be one of the most important tools in the nanotechnology bottom-up[1] revolution.

The relevant interactions for SFM modeling are discussed, and methods to calculate them at *ab initio* and atomistic levels are presented in this thesis. In order to calculate the van der Waals and capillary interactions in larger scale phenomena, continuum methods are also developed. Models of the SFM tip and surfaces are presented, and methods to combine tip-sample interactions and knowledge of realistic SFM cantilever dynamics into a realistic simulation of SFM imaging are introduced.

The methods are applied to study different problems in scanning force microscopy, and new conclusions have arisen: The continuum model for capillary forces presented in Publication **II** has shown how the behavior of capillary meniscus formation changes at the nanoscale, relevant for scanning force microscopy experiments in a humid ambient, and how a strong humidity dependence on capillary forces arises instead of an almost humidity independent behavior observed in the macroscopic world. Modeling scanning force microscopy imaging of flat surfaces in atomic resolution has given new tools for identification of surface species on metal oxide (Publication **I**) and alkali halide (Publication **IV**) insulator surfaces, and provided new knowledge on applicability of different types of SFM tip models in simulations. Simulated imaging of gold and palladium clusters on insulating substrates, presented in Publications **III**, **IV** and **V** has revealed origins of experimental difficulties in obtaining reasonable image contrast on clusters, both with *ab initio* atomic scale simulations and with larger scale continuum simulations. In this context a novel application to image clusters in a higher detail than previously possible, utilizing the constant height mode of scanning force microscopy, was developed. All in all, the results show how close collaboration between experiment and theory can benefit both, and how a wide variety of phenomena from details of electronic structure in atoms to water menisci, tens of nanometers in diameter, affect the same instrument, the scanning force microscope.

---

[1] Building structures atom by atom or by self-assembly, opposite to top-down approach like lithographic methods.

Experimental as well as theoretical work on SFM is gradually turning from imaging stable surfaces and structures in UHV into other areas. Imaging structures will be complemented by manipulation of atoms or molecules. More research will be done outside UHV conditions, for example when imaging biological molecules in their natural environment (air or water) with an ever-increasing resolution. Interpreting surface images is complemented by establishing new ways of chemical identification, like force spectroscopy or detecting dissipation. These new realms of science by SFM broaden the scope of the technique, but most of this work at the atomic scale is still limited by a common challenge, the uncertainty of tip structure in the experiment. More advanced methods to circumvent the problem, either by experimental tip preparation, functionalization and cleaning, or by utilizing the increasing computational power to characterize measured images or frequency shift - distance curves in a more automated way, are thus needed to make scanning force microscope the very powerful, fast and unambiguous instrument it is about to become.

Bibliography

[1] H. P. Lang, R. Berger, F. Battiston, J.-P. Ramseyer, E. Meyer, C. Andreoli, J. Brugger, P. Vettiger, M. Despont, T. Mezzacasa, L. Scandella, H.-J. Güntherodt, C. Gerber, and J. K. Gimzewski, Appl. Phys. A **66**, S61 (1998).

[2] Probe storage: The Millipede project. A nanomechanical AFM-based data storage system, `http://www.zurich.ibm.com/st/storage/index.html`, [cited 5.9.2007].

[3] S. Morita, R. Wiesendanger, and E. Meyer, *Noncontact Atomic Force Microscopy* (Springer, Berlin, 2002).

[4] F. J. Giessibl, Rev. Mod. Phys. **75**, 949 (2003).

[5] W. A. Hofer, A. S. Foster, and A. L. Shluger, Rev. Mod. Phys. **75**, 1287 (2003).

[6] R. García and R. Pérez, Surf. Sci. Rep. **47**, 197 (2002).

[7] G. Binnig and H. Rohrer, Rev. Mod. Phys. **71**, S324 (1999).

[8] A. S. Foster and W. A. Hofer, *Scanning Probe Microscopy* (Springer, New York, 2006).

[9] G. Binnig, C. Quate, and C. Gerber, Phys. Rev. Lett. **56**, 930 (1986).

[10] The Nobel Prize in Physics 1986, `http://nobelprize.org/nobel_prizes/physics/laureates/1986/index.html`, [cited 5.9.2007].

[11] G. Binnig and H. Rohrer, Helv. Phys. Acta **55**, 726 (1982).

[12] H. Neddermeyer, Rep. Prog. Phys. **59**, 701 (1996).

[13] F. Besenbacher, Rep. Prog. Phys. **59**, 1737 (1996).

[14] D. Eigler and E. Schweizer, Nature **344**, 524 (1990).

[15] C. R. Henry, Surf. Sci. Rep. **31**, 231 (1998).

[16] V. E. Henrich and P. A. Cox, *The Surface Science of Metal Oxides* (Cambridge University Press, Cambridge, 1996).

[17] *Nanocatalysis*, edited by U. Heiz and U. Landman (Springer-Verlag, Berlin Heidelberg, 2007).

[18] M. Dragoman and D. Dragoman, *Nanoelectronics: Principles and Devices* (Artech House, Norwood, 2006).

[19] M. Bäumer and H.-J. Freund, Prog. Surf. Sci. **61**, 127 (1999).

[20] S. Hembacher, F. J. Giessibl, and J. Mannhart, Science **305**, 380 (2004).

[21] F. J. Giessibl, Phys. Rev. B **56**, 16010 (1997).

[22] J. Preiner, J. Tang, V. Pastushenko, and P. Hinterdorfer, Phys. Rev. Lett. **99**, 046102 (2007).

[23] F. J. Giessibl and C. F. Quate, Physics Today **59**, 44 (2006).

[24] U. Dürig, New J. Phys. **2**, 1 (2000).

[25] R. Bennewitz, A. S. Foster, L. N. Kantorovich, M. Bammerlin, C. Loppacher, S. Schär, M. Guggisberg, E. Meyer, and A. L. Shluger, Phys. Rev. B **62**, 2074 (2000).

[26] M. Gauthier and M. Tsukada, Phys. Rev. B **60**, 11716 (1999).

[27] L. N. Kantorovich, Phys. Rev. Lett. **89**, 096105 (2002).

[28] T. Trevethan and L. Kantorovich, Phys. Rev. B **70**, 115411 (2004).

[29] L. N. Kantorovich and T. Trevethan, Phys. Rev. Lett. **93**, 236102 (2004).

[30] C. L. Pang, A. Sasahara, H. Onishi, Q. Chen, and G. Thornton, Phys. Rev. B **74**, 073411 (2006).

[31] Y. Sugimoto, P. Pou, M. Abe, P. Jelinek, R. Pérez, S. Morita, and O. Custance, Nature **446**, 64 (2007).

[32] A. S. Foster, *Theoretical Modelling of Non-contact Atomic Force Microscopy on Insulators*, PhD thesis, University College London, 2000, `http://www.fyslab.hut.fi/∼asf/physics/thesis1/thesis1.html`.

[33] A. L. Shluger, A. L. Rohl, D. H. Gay, and R. T. Williams, J. Phys.: Condens. Matter **6**, 1825 (1994).

[34] A. I. Livshits and A. L. Schluger, Faraday Discuss. **106**, 425 (1997).

[35] S. R. Elliott, *The Physics and Chemistry of Solids* (John Wiley & Sons, Chichester, 2000).

[36] A. Ŝarlah and S. Ẑumer, Phys. Rev. E **64**, 051606 (2001).

[37] J. Israelachvili, *Intermolecular and Surface Forces* (Academic Press, London, 1991).

[38] H. C. Hamaker, Physica **4**, 1058 (1937).

[39] E. M. Lifshitz, Soviet Phys. JETP **2**, 73 (1956).

[40] H. B. G. Casimir, Koninkl. Ned. Akad. Wetenschap. Proc. **51**, 793 (1948).

[41] O. H. Pakarinen, A. S. Foster, M. Paajanen, T. Kalinainen, J. Katainen, I. Makkonen, J. Lahtinen, and R. M. Nieminen, Modelling Simul. Mater. Sci. Eng. **13**, 1175 (2005).

[42] K. Mukasa, H. Hasegawa, Y. Tazuke, K. Sueoka, M. Sasaki, and K. Hayakawa, Jpn. J. Appl. Phys. **33(5A)**, 2692 (1994).

[43] K. Sueoka, A. Subagyo, H. Hosoi, and K. Mukasa, Nanotechnology **15**, S691 (2004).

[44] O. H. Pakarinen and A. S. Foster, in preparation.

[45] C. Fiolhais, F. Noqueira, and M. Marques, *A Primer in Density Functional Theory* (Springer-Verlag, Berlin, Heidelberg, New York, 2003).

[46] R. M. Martin, *Electronic Structure* (Cambridge University Press, Cambridge, 2004).

[47] P. Hohenberg and W. Kohn, Phys. Rev. **136**, 864 (1964).

[48] W. Kohn and L. Sham, Phys. Rev. **140**, 1133 (1965).

[49] D. M. Ceperley and B. J. Alder, Phys. Rev. Lett. **45**, 566 (1980).

[50] J. P. Perdew, K. Burke, and M. Ernzerhof, Phys. Rev. Lett. **77**, 3865 (1996).

[51] J. P. Perdew, J. A. Chevary, S. H. Vosko, K. A. Jackson, M. R. Pederson, D. J. Singh, and C. Fiolhais, Phys. Rev. B **46**, 6671 (1992).

[52] A. D. Becke, Phys. Rev. A **38**, 3098 (1988).

[53] C. Lee, W. Yang, and R. G. Parr, Phys. Rev. B **37**, 785 (1988).

[54] P. Bagno, O. Jepsen, and O. Gunnarsson, Phys. Rev. B **40**, 1997 (1989).

[55] Reprinted with permission from M. C. Payne, M. P. Teter, D. C. Allan, T. A. Arias and J. D. Joannopoulos, Rev. Mod. Phys. **64**, 1045 (1992). Copyright (1992) by the American Physical Society.

[56] J. C. Phillips, Phys. Rev. **112**, 685 (1958).

[57] K. E. Atkinson, *An introduction to numerical analysis* (Wiley & Sons, New York, 1989).

[58] J. Hellmann, *Einführung in die Quantenchemie* (Deuticke, Liepzig, 1937).

[59] R. P. Feynman, Phys. Rev. **56**, 340 (1939).

[60] P. Pulay, Molec. Phys. **19**, 197 (1969).

[61] P. Ordejón, E. Artacho, and J. M. Soler, Phys. Rev. B **53**, R10441 (1996).

[62] J. M. Soler, E. Artacho, J. D. Gale, A. García, J. Junquera, P. Ordejón, and D. Sánchez-Portal, J. Phys.: Condens. Matter **14**, 2745 (2002).

[63] L. Kleinman and D. M. Bylander, Phys. Rev. Lett. **48**, 1425 (1982).

[64] B. G. Dick and A. W. Overhauser, Phys. Rev. **112**, 603 (1958).

[65] A. L. Shluger, A. L. Rohl, D. H. Gay, and R. T. Williams, J. Phys.: Condens. Matter **6**, 1825 (1994).

[66] K. Ohno, K. Esfarjani, and Y. Kawazoe, *Computational Materials Science* (Springer, Berlin, 1999).

[67] K. Cooper, A. Gupta, and S. Beaudoin, J. Colloid Interface Sci. **234**, 284 (2001).

[68] F. M. Orr, L. E. Scriven, and A. P. Rivas, J. Fluid Mech. **67**, 723 (1975).

[69] A. W. Adamson, *Physical Chemistry of Surfaces*, 3rd ed. ed. (Wiley, New York and London, 1976).

[70] M. Paajanen, J. Katainen, O. H. Pakarinen, A. S. Foster, and J. Lahtinen, J. Colloid Interface Sci. **304**, 518 (2006).

[71] X. Xiao and L. Qian, Langmuir **16**, 8153 (2000).

[72] N. R. Tas, P. Mela, T. Kramer, J. W. Berenschot, and A. van den Berg, Nano Letters **3**, 1537 (2003).

[73] Q. Zheng, D. J. Durben, G. H. Wolf, and C. A. Angell, Science **254**, 829 (1991).

[74] A. S. Foster, O. H. Pakarinen, J. M. Airaksinen, J. D. Gale, and R. M. Nieminen, Phys. Rev. B **68**, 195410 (2003).

[75] Reprinted from N. D. McCavish and R. A. Bennett, Surf. Sci. **546**, 47 (2003) with permission from Elsevier.

[76] A. S. Foster, A. Y. Gal, J. M. Airaksinen, O. H. Pakarinen, Y. J. Lee, J. D. Gale, A. L. Shluger, and R. M. Nieminen, Phys. Rev. B **68**, 195420 (2003).

[77] J. V. Lauritsen, A. S. Foster, G. H. Olesen, M. C. Christensen, A. Kühnle, S. Helveg, J. R. Rostrup-Nielsen, B. S. Clausen, M. Reichling, and F. Besenbacher, Nanotechnology **17**, 3436 (2006).

[78] H.-J. Freund, Surf. Sci. **500**, 271 (2002).

[79] M. Haruta, N. Yamada, H. Kobayashi, and S. Iijima, J. Catal. **115**, 301 (1989).

[80] M. Valden, X. Lai, and D. W. Goodman, Science **281**, 1647 (1998).

[81] V. Bondzie, S. C. Parker, and C. T. Campbell, Catal. Lett. **63**, 143 (1999).

[82] H. Häkkinen, W. Abbet, A. Sanchez, U. Heiz, and U. Landman, Angew. Chem., Int. Ed. **42**, 1297 (2003).

[83] C. T. Campbell, Science **306**, 234 (2004).

[84] B. Yoon, H. Häkkinen, U. Landman, A. S. Wörz, J. M. Antonietti, S. Abbet, K. Judai, and U. Heiz, Science **307**, 403 (2005).

[85] S. N. Rashkeev, A. R. Lupini, S. H. Overbury, S. J. Pennycook, and S. T. Pantelides, Phys. Rev. B **76**, 035438 (2007).

[86] C. Barth and C. R. Henry, Nanotechnology **15**, 1264 (2004).

[87] O. H. Pakarinen, C. Barth, A. S. Foster, R. M. Nieminen, and C. R. Henry, Phys. Rev. B **73**, 235428 (2006).

[88] D. J. Wales, J. P. K. Doye, A. Dullweber, M. P. Hodges, F. Y. Naumkin, F. Calvo, J. Hernández-Rojas, and T. F. Middleton, The Cambridge Cluster Database, `http://www-wales.ch.cam.ac.uk/CCD.html`, [cited 13.9.2007].

[89] R. Hoffmann, L. N. Kantorovich, A. Baratoff, H. J. Hug, and H.-J. Güntherodt, Phys. Rev. Lett. **92**, 146103 (2004).

[90] K. G. Huang, D. Gibbs, D. M. Zehner, A. R. Sandy, and S. G. J. Mochrie, Phys. Rev. Lett. **65**, 3313 (1990).

[91] C. Barth, O. H. Pakarinen, A. S. Foster, and C. R. Henry, Nanotechnology **17**, S128 (2006).

[92] H. Graoui, S. Giorgio, and C. R. Henry, Phil. Mag. B **81**, 1649 (2001).

[93] J. Goniakowski and C. Mottet, J. Cryst. Growth **275**, 29 (2005).

[94] N. I. Papanicolaou and D. A. Papaconstantopoulos, Thin Solid Films **428**, 40 (2003).